

RESEARCH ARTICLE | OCTOBER 27 2022

Direct numerical simulation of supersonic bump flow with shock impingement

Jiang Lai (赖江); Zhaolin Fan (范召林); Siwei Dong (董思卫); ... et. al



Physics of Fluids 34, 105131 (2022)

<https://doi.org/10.1063/5.0106488>



View
Online



Export
Citation

CrossMark

Articles You May Be Interested In

Delayed mechanical failure of the under-bump interconnects by bump shearing

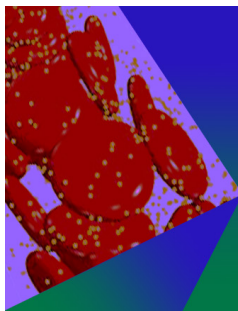
Journal of Applied Physics (April 2012)

Studies of beam injection with a compensated bump and uncompensated bump in a synchrotron

Rev Sci Instrum (August 2013)

The influence of speed bumps on perceived annoyance

J Acoust Soc Am (May 2008)



Physics of Fluids

Special Topic: Flow and Forensics

Submit Today!

Direct numerical simulation of supersonic bump flow with shock impingement

Cite as: Phys. Fluids **34**, 105131 (2022); doi: 10.1063/5.0106488

Submitted: 28 June 2022 · Accepted: 20 September 2022 ·

Published Online: 27 October 2022







View Online



Export Citation



CrossMark

Jiang Lai (赖江),^{1,2}  Zhaolin Fan (范召林),³ Siwei Dong (董思卫),^{1,2}  Xinliang Li (李新亮),^{4,5} 
Fulin Tong (童福林),^{1,2,a)}  and Xianxu Yuan (袁先旭)^{1,2,a)} 

AFFILIATIONS

¹State Key Laboratory of Aerodynamics, China Aerodynamics Research and Development Center, 621000 Mianyang, China

²Computational Aerodynamics Institute of China, Aerodynamics Research and Development Center, 621000 Mianyang, China

³China Aerodynamics Research and Development Center, 621000 Mianyang, China

⁴LHD, Institute of Mechanics, Chinese Academy of Sciences, 100190 Beijing, China

⁵School of Engineering Science, University of Chinese Academy of Sciences, 100049 Beijing, China

^{a)} Authors to whom correspondence should be addressed: 515363491@qq.com and yuanxianxu@cardc.cn

ABSTRACT

Direct numerical simulations are carried out to identify the effects of shock impingement on the behavior of bump flow at freestream Mach number of 2.25. Two cosine-shaped bump cases, with and without an impinging oblique shock at an angle of 33.2° , are compared. The shock impingement exhibits a remarkable influence on the pattern of the shock system and on the size of the separation region. A spectral analysis finds that low-frequency unsteadiness is significantly enhanced by the impingement interaction, and the proper orthogonal decomposition highlights the low-frequency breathing motion of the separation bubble, which is accurately reconstructed using only the first ten low-order modes. Downstream of the bump, both the Reynolds stress components and the turbulence kinetic energy exhibit a general amplification, with the peaks reoccurring at outer wall-normal locations. A turbulent kinetic energy budget analysis shows the greatly increased production in the outer layer which is balanced by turbulent transport and dissipation. An anisotropy-invariant map analysis identifies enhanced isotropic turbulence in the vicinity of the bump, which is qualitatively modified into a two-component axisymmetric state around the reattachment point. In addition, the mean skin friction decomposition suggests that the shock impingement has little influence on the predominant contribution of turbulence kinetic energy production, apart from the spatial growth dominance at the bump summit in the absence of the impinging shock. Interestingly, a scale-decomposed analysis quantitatively demonstrates that the contributions of small-scale structures are attenuated, but those of large-scale ones are relatively increased, with a contribution of more than 80% with shock impingement.

Published under an exclusive license by AIP Publishing. <https://doi.org/10.1063/5.0106488>

I. INTRODUCTION

Interactions between shock waves and turbulent boundary layers (SWBLIs) are common in both internal and external flows of aircraft. Extensive investigations have been carried out on this topic since Ferri¹ first observed the phenomenon on airfoil surfaces when performing a high-speed wind tunnel test. The complicated flow behaviors, including shock oscillation, separation and reattachment, turbulence amplification, vortex evolution, and so forth, are commonly found in the interaction region, leading to strong pressure fluctuations, severe peak heating, and poor skin friction distribution. These may constitute a threat to aerodynamic characteristics, structural integrity, and flight safety in high-speed aircraft.^{2,3} To avoid the negative effects of SWBLI on the performance of high-speed vehicles, several passive and active strategies are proposed, for example, using a

bump is a potential flow control device for SWBLI in internal flows, which could effectively prohibit flow separation in supersonic/hypersonic inlets and improve efficiency, depending on the wise design of incident positions. However, there is the potential to improve the mixture of fuels inside the combustor and break dangerous flows.⁴ Therefore, understanding the flow mechanism in the shock interaction region is of great importance and is becoming significantly urgent as hypersonic vehicles are rapidly being developed.

Tremendous progress has been made in understanding fundamental issues in the SWBLI problem by means of numerical and experimental studies on incident shock interactions and compression corner interactions,⁵ and some controversial subjects, such as the origin of low-frequency shock oscillation, the source of turbulence amplification, and the generation mechanism of the skin friction, remain to

be explained. For example, Clemens and Narayanaswamy⁶ reviewed the possible causes of low-frequency unsteadiness and categorized the reasons into upstream mechanisms, downstream mechanisms, and a combination of the two, depending on the separation state. Specifically, Chan *et al.*⁷ operated planar laser Mie scattering technology on a compression corner and identified the dependency of its effects on the thickness of the upstream boundary layer. Beresh *et al.*⁸ used particle image velocimetry to demonstrate the shape of the velocity profiles as the main inducement. Andreopoulos and Muck⁹ found the shock oscillation frequency to be comparable with the upstream turbulence burst frequency, although Thomas *et al.*¹⁰ found contrasting experimental results. Toubert and Sandham¹¹ presented a large eddy simulation (LES) study on an incident shock interaction, showing the driving mechanism related to the global-mode instability of the separation bubble. A direct numerical simulation (DNS) carried out by Priebe and Martin¹² on a compression corner suggested that a change in low-pass filtered flow was caused by inherent instability in the downstream separated flow, which was related to separation bubble breathing. In addition, Grilli *et al.*¹³ reported a satisfactory reconstruction of separation bubble motion using four low-frequency modes in dynamic mode decomposition of the compression corner flow at Mach 2.88, confirming the low-frequency unsteadiness of the separated interaction flow.

Turbulence amplification in SWBLI has been extensively investigated via DNS, with the full-scale turbulent flow details provided.¹⁴ Studying an incident shock interaction at Mach 2.25, Fang *et al.*¹⁴ found that the interaction between mean flow deceleration and streamwise velocity fluctuations was responsible for the increased turbulence intensity in the upstream region, and the free-shear layer controlled the amplification of the downstream region. Adams¹⁵ proposed an amplification factor of 4 at Mach 3 for the compression corner interactions, and this coincided with the results obtained by Smits and Muck¹⁶ in a wind tunnel experiment at Mach 2.9. Wu and Martin¹⁷ found peak turbulence kinetic energy (TKE) in the near-wall region of the boundary layer, where the amplification was due to the comprehensive effects of an R–H jump across the shock wave, the nonlinear coupling of turbulence, vorticity, entropy waves, and the unsteady shock wave pumping effect. Priebe and Martin¹² showed that the maximum TKE occurred in the middle of the shear layer, with enhanced structures in the detached shear layer shedding downward. Helm *et al.*¹⁸ concluded that the generation of large-scale vortices in the free-shear layer was a major mechanism of turbulence amplification, which was supported by Tong *et al.*,¹⁹ who observed large-scale hairpins and packets along with broken streaks in the near-wall region of the boundary layer. It should be noted that the amplification of the wall turbulence analyzed in that study had regular configurations; however, in any engineering context, perturbations, such as pressure gradient, surface curvature, roughness, and so forth, are to be expected, and a comprehensive understanding of complex geometries (i.e., concave and convex surfaces or grooves and wavy walls) is needed.

Relatively fewer investigations of practical complex geometries, such as bump flow, have been carried out, due to the difficulty in predicting the variation in the pressure gradient, separations, and curvature effects. Cavar and Meyer²⁰ identified the constantly changing pressure gradient over a bump, where the adverse pressure gradient (APG) in the bump upstream region changes to a favorable pressure gradient (FPG) approaching the summit; then, it returns to APG at

the rear part of the bump and ultimately ends with an FPG in the downstream region. Tsuji and Morikawa²¹ and Baskaran *et al.*²² found that the logarithmic law breaks down in the strong FPG region. Balin and Jansen²³ analyzed APG-induced separation and FPG-related reattachment in an incompressible flow over a Gaussian-shaped bump. Webster *et al.*²⁴ identified an independent internal layer beneath the turbulent free shear in an experiment with a curved hill. Their results were confirmed by Wu and Squires²⁵ through the LES approach, as a consequence of selectively altered turbulence shear stress due to quasi-step increases at the leading and trailing edges of the bump. Baskaran *et al.*²⁶ reported a dominant curvature effect in the outer boundary layer and a pressure gradient that originated from the inner layer through a decoupled process for the transportation of the TKE.

With an incident shock introduced into the bump flow, streamwise pressure gradient and the shock system are dramatically changed, which is different from those in ideal canonical configurations for SWBLI problems. Investigating the case of the shock interactions, Lawal and Sandham²⁷ studied the interactions between shock and a laminar boundary layer over a Delery bump using DNS. Sandham *et al.*²⁸ numerically tested normal shock effects on a transonic turbulent boundary layer over a circular-arc bump through LES, accompanied by a discussion of decay and amplification in the turbulence fluctuations. Sartor *et al.*²⁹ conducted a wind tunnel experiment in a transonic channel flow over a shock-generation bump and investigated unsteadiness and global stability in the interaction region, finding different temporal scales of unsteadiness in the shock and mixing layer and identifying a relationship between shock motion and the expansion and contraction of the recirculation bubble. The above-mentioned case of bump-induced shocks showed more complex unsteady characteristics than the basic bump flows. To the best of our knowledge, the incident shock waves interacting with the bump flows have not been adequately investigated, which has led to a deficient understanding of the SWBLI problem over a bump.

Therefore, the objective of this paper is to systematically evaluate the effects of an impinging oblique shock on a supersonic cosine-shaped bump flow adopting the DNS approach. Two cases are considered. The first is *with shock* (WS) and contains a bump with an impinging oblique shock, while the second, *shock free* (SF), exhibits a basic bump flow for comparison. This study investigates the affected flow regimes, separation bubble, turbulence statistics, and the generation mechanism of skin friction in these cases.

The remainder of this paper proceeds as follows: The computation model and general setups for the DNS calculations are presented in Sec. II. Upstream turbulent boundary layer (TBL) is validated in this part. In Sec. III, we discuss the incident shock effects on the flow characteristics and the generation mechanism of the skin friction. Finally, concluding remarks are provided in Sec. IV.

II. SIMULATION SETUP

A. Computation overview

The flow configuration, which is composed of two parts, is shown in Fig. 1. First, the base is a horizontally positioned flat plate shown on the x – z plane. The size of the foundation is $L_x \times L_z = 137.6 \times 4.4 \text{ mm}^2$, where x and z present the streamwise and spanwise directions, respectively. The base is extruded for $L_y = 12.7 \text{ mm}$ along the wall-normal direction, forming a cuboid computation domain.

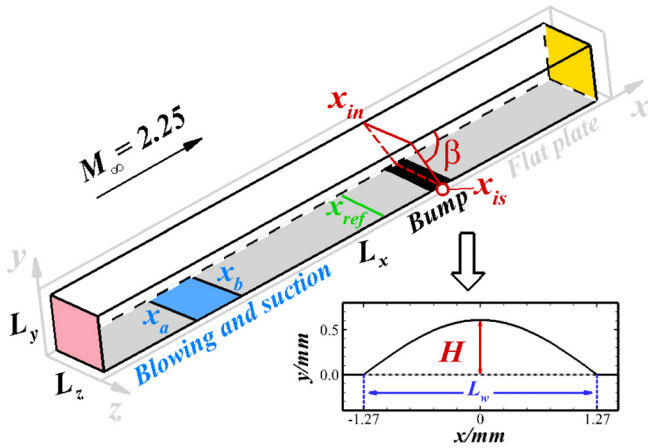


FIG. 1. Overall computation domain and a close-up side view of the bump. The flat plate is colored in light gray, the bump is highlighted in black, the reference station is labeled in green, the blowing and suction region is colored in blue, the inlet and outlet are colored in pink and yellow, respectively.

Second, a local bump in a half-cosine shape being 111.76 mm downstream from the domain inlet is subtracted from the domain, where the bump would be located in a fully developed turbulent flow for the considered SWBLI study. It has a length of $L_w = 2.54$ mm with an amplitude of $H = 0.61$ mm, which is 3/10 of the boundary layer thickness at the reference station $x_{ref} = -17.78$ mm when the origin is designated to be right at the projected bump center. The bump amplitude is determined to show obvious effects on the interaction characteristics, as suggested by Tong *et al.*³⁰ and Zhang *et al.*³¹ in the investigations on a wavy wall and a bump with the height about 0.3 times of the upstream boundary layer thickness. To create a turbulent flow, the region from $x_a = -104.14$ mm to $x_b = -91.44$ mm is triggered using a blowing and suction method. In case WS, an incident shock at an angle of $\beta = 33.2^\circ$ is shot from the upper boundary at $x_{in} = -19.41$ mm, and therefore the nominal impinging point is at $x_{is} = 0$ mm. More details of turbulence creation and shock introduction are provided in Sec. II B.

Figure 2 presents a side view of the overall grid and a close-up view of the grid around the bump. To capture precise flow features of the interaction, 3600 points are equally spaced in the region $-35.6 < x < 25.4$ mm along the flow direction. A progressively refined grid with 600 points is assigned in the region $-101.6 < x < -35.6$ mm, while 100 gradually coarsened points with a grid growth ratio of 1.03 are added to the region $25.4 < x < 35.6$ mm. In the wall-normal direction, 300 points are clustered that obey hyperbolic tangent mapping to the wall. Therefore, about 200 points are guaranteed to fall inside the upstream TBL. A uniformly distributed grid is applied in the spanwise direction. In all, $N_x \times N_y \times N_z = 4300 \times 300 \times 250$ points are used in the present simulations. Normalized by wall units at x_{ref} the spatial resolutions of the grid within the interaction region are $\Delta x^+ = 5.6$, $\Delta y_w^+ = 0.66$, $\Delta y_e^+ = 11.3$, and $\Delta z^+ = 6.6$, respectively. Superscript + indicates a normalized length scale by friction velocity u_τ and the viscous coefficient ν_w on the wall. Subscripts w and e represent the wall and the boundary layer edge, respectively.

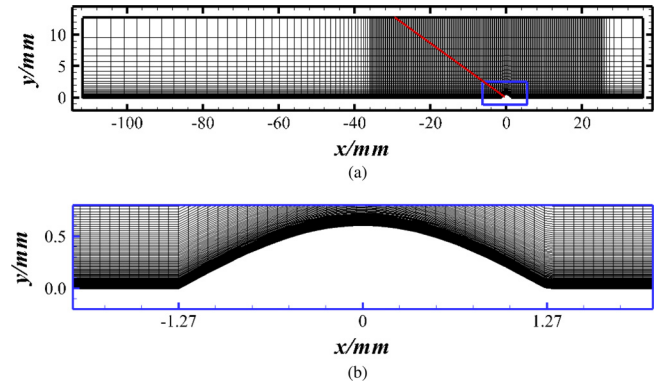


FIG. 2. Computational grid sketches: (a) overall grid (plotted at every 10 and 5 points along the x and y directions, respectively); (b) enlarged grid around the bump.

B. Numerical methodology

OpenCFD-SC, an open-source finite-difference DNS high-fidelity code that has been extensively validated, is used to perform the calculations and identify the three-dimensional compressible Navier–Stokes equations for ideal gas in curvilinear coordinates. The incoming free-stream flow parameters are used to nondimensionalize the governing equation. The dynamic viscosity coefficient is determined by Sutherland’s law. As is well-known, accuracy and robustness of numerical schemes are critical to turbulent simulations. In particular, the turbulent flows exhibit strong unsteady fluctuations and are characterized by a wide range of flow scales. The sudden discontinuity caused by the shock waves makes the situation even more complex. In addition, potential separation with shock oscillation demands strong and robust discretization schemes. Therefore, for spatial terms, the optimized weighted essentially non-oscillation scheme proposed by Martin *et al.*³² is selected for the convective term. This is a fourth-order and bandwidth-optimized scheme with a limiter to deal with SWBLI problems. The viscous term employs a general eighth-order central difference scheme. The third-order total variation diminishing (TVD) Runge–Kutta method is adopted to advance time integration at a pace of $\Delta t U_\infty / \delta = 0.0125$. The incoming freestream flow parameter includes a Mach number of $M_\infty = 2.25$, a unit Reynolds number of $Re_\infty / \text{mm} = 2.5 \times 10^4$, and a static temperature of $T_\infty = 169.44$ K. In case WS, instead of using a shock generator, an incident shock is produced by imposing the flow parameters, using single-point Rankine–Hugoniot relations based on the freestream Mach number and the angle of impingement on the upper boundary of the computational domain. The normalized parameters that follow the shock wave are 1.397, 0.915, -0.130 , and 1.148 for density, streamwise velocity, normal velocity, and temperature, respectively. The 33.2° impinging shock is typical to investigate the reflected interactions in the separated turbulent boundary layer at Mach 2.25, which is a commonly used condition for SWBLI investigations by means of wind tunnel experiments and numerical simulations.^{14,35} Unless otherwise stated, the Reynolds average generic variable f is denoted as \bar{f} , while the Favre average is written as \tilde{f} . The corresponding fluctuations are represented by f' and f'' , respectively.

Regarding the boundary conditions, a laminar profile turns on the flowfield at the entrance. This profile is obtained from a laminar

TABLE I. TBL parameters at the reference station x_{ref} .

Case	M_∞	Re_δ	Re_{δ^*}	Re_θ
SF (present DNS)	2.25	51 088	11 779	3545
WS (present DNS)	2.25	50 800	11 636	3524
Tong <i>et al.</i> ³³	2.25	51 087	11 840	3567
Fang <i>et al.</i> ¹⁴	2.25	51 468	12 216	3700

solution of a boundary layer under the same flow conditions. A supersonic outlet, together with a buffer region, is designed at the exit. A nonreflecting condition is arranged at the top border in both cases and the incident shock condition is employed only in case WS to generate the upstream incident shock. The whole bottom base is an isothermal no-slip wall of $T_w/T_\infty = 1.9$. As noted in Sec. II A, the blowing and suction area is attached to the flat plate by arranging the same random normal velocity disturbance as Fang *et al.*,¹⁴ where the amplitude is $A = 0.2U_\infty$ and the frequency is $\omega = 0.628U_\infty/\delta$. In this way, a laminar flow is disrupted and begins to transit. A fully developed TBL is expected to be offered at least before the reference station x_{ref} . This is examined in Sec. II C by comparing the velocity profiles and turbulence features with those reported in the literature. The periodic condition is applied to both sidewalls. The flow-through time, denoted as L_x/U_∞ , represents the time required to sweep the computational domain along the freestream direction at a velocity of U_∞ . At least double the flow-through time is required before a turbulent statistically steady state can be achieved. As such, 200 instantaneous flows are sampled, with a total collection time of $TU_\infty/\delta = 250$.

C. Validation

To test the generation of the TBL, the velocity and turbulence characteristics at the reference station x_{ref} are compared with the previous studies. The boundary layer, displacement, and momentum thicknesses are $\delta = 2.03$ mm, $\delta^* = 0.47$ mm, and $\theta = 0.14$ mm, respectively. The corresponding Reynolds number is shown in Table I. The TBL parameters are found to be in good agreement with the results obtained by Tong *et al.*³³ and Fang *et al.*¹⁴ under the same conditions.

Both velocity profiles in Fig. 3 match well with those in the literature.^{14,33,34} Panel (a) shows the wall-normal profiles of the mean streamwise velocity, and the Van Driest transformed mean streamwise velocity profiles in panel (b) obey the classic law of wall features. For instance, the linear law is satisfied in the viscous sublayer when $y^+ < 10$, after which the logarithmic law functions at $30 < y^+ < 100$. The distributions of turbulence statistics in inner scaling at the reference station x_{ref} are presented in Fig. 4. Panel (a) displays the wall-normal profiles of the Reynolds stress R_{ij} , which is normalized by the square of friction velocity u_τ . A satisfactory agreement in the Reynolds stress components is found when compared with that obtained by Fang *et al.*¹⁴ and Tong *et al.*³³ The peak of R_{11} is located around $y^+ = 13$, in agreement with Pirozzoli and Grasso.³⁵ Density-weighted turbulence intensity is shown in panel (b). The subscript w indicates a variable at the wall, and rms denotes the root mean square of the variable. The results are quantitatively consistent with Pirozzoli *et al.*³⁶ and Tong *et al.*³³ As the compressible effects are limited under the present freestream Mach number, the results also coincide with those in incompressible TBLs proposed by Spalart³⁷ and Wu and Moin.³⁸ As such, a reliable fully developed TBL is well established in the present simulations and can be used for further analysis.

The bump flow with the shock impingement is validated through a grid sensitivity study. Based on the computational grid described in Sec. II A, a refined grid is designed by increasing the grid points in the spanwise and the streamwise directions in the interaction region to 150% of the original ones. Therefore, the total grid points are $N_x \times N_y \times N_z = 6100 \times 300 \times 375$ (the refined case is denoted as $6100 \times 300 \times 375$ in Fig. 5, where the original case with $N_x \times N_y \times N_z = 4300 \times 300 \times 250$ is represented by $4300 \times 300 \times 250$), and the corresponding grid resolutions in wall unit are $\Delta x^+ = 5.6$ and $\Delta z^+ = 6.6$ in the streamwise and spanwise directions, respectively. Figure 5 compares the distribution of the mean skin friction and surface pressure in the streamwise direction between the two cases. The relative differences of the skin friction between the two cases are less than 4% around the bump, and no obvious discrepancy is observed in the pressure curves, indicating that the original grid is sufficient to obtain accurate results. All of the analysis of case WS in this paper is based on the original grid. The most important feature of the bump flow, the streamwise pressure distribution, is described in Fig. 5(b),

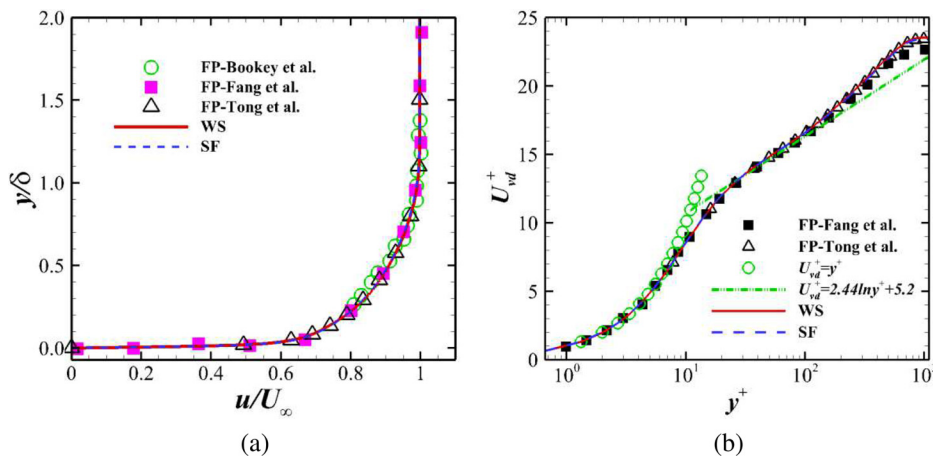


FIG. 3. Comparison of streamwise velocity with literature at the reference station x_{ref} . (a) normalized streamwise velocity profile; (b) Van Driest transformed streamwise velocity.

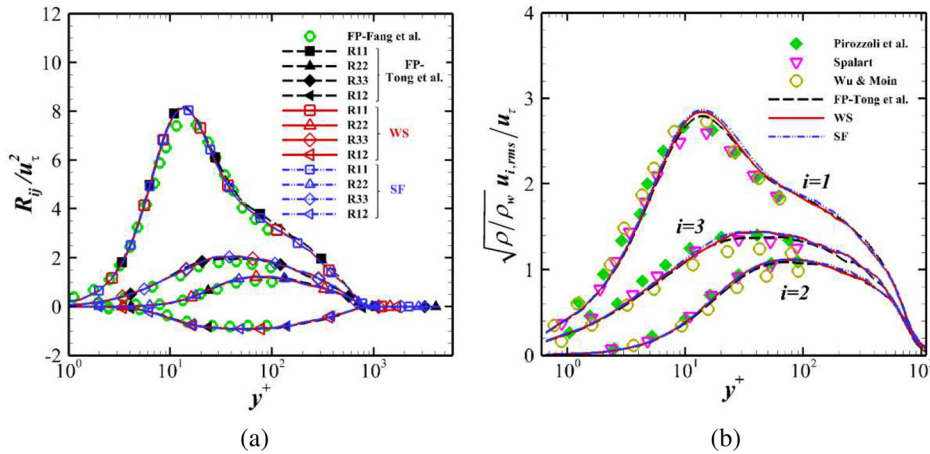


FIG. 4. Comparison of turbulence statistics with the results in the literature at the reference station x_{ref} . (a) Reynolds stress components R_{ij} ; (b) density-weighted turbulence intensity.

where two pressure rises (associated with the incident shock and separation) and one pressure drop (caused by the bump-induced expansion waves) are well captured along the bump in the interaction region, corresponding to the typical variation of surface pressure over a similar supersonic bump geometry obtained by Zhang *et al.*³¹ through wind tunnel experiments. Therefore, it is reasonable to conclude that the bump flow with the shock impingement is satisfactorily resolved based on the numerical methodology in the present study.

III. RESULTS AND DISCUSSION

A. Instantaneous and mean flowfields

Figure 6 shows the instantaneous density gradient field in the middle $x-y$ plane, where the variable defined as

$$N_s = 0.8e^{-10(\nabla\rho - \nabla\rho_{min})/(\nabla\rho_{max} - \nabla\rho_{min})} \quad (1)$$

is used. Here, $\nabla\rho_{max}$ and $\nabla\rho_{min}$ are the maximum and minimum values of the density gradient $\nabla\rho$, respectively. The impinging shock significantly destroys the shock system, where two interesting observations are highlighted in Fig. 6. First, shock 1 is replaced by the reflected shock, and the separation shock shifts upward. This could be related to the enlarged separation region around the upstream side of

the bump, which is further discussed in the following analysis. Second, shock 2, at the downstream of the bump trailing edge, is apparently weakened and converted into a series of compression waves.

A three-dimensional view of the affected instantaneous flowfield is shown in Fig. 7. When subjected to shock 1 shown in Fig. 7(a), vortical structures that originate from the upstream TBL are more frequently observed and are lifted up, approaching the leading edge of the bump. In the downstream region where shock 2 appears, the near-wall vortical structures are found to be weakened compared with those along the front bump surface. Likewise, as shown in Fig. 7(b), the large-scale vortical structures in the outer layer are greatly strengthened after they pass through the incident and reflected shocks. However, the heightened structures are preserved and last longer in the streamwise direction from the trailing edge of the bump in the downstream region, due to the more severe disturbance from the strong shock impinging effects. One possible reason for the delayed restoration may be associated with the downstream separation flow.

The separation induced by the shock waves can be illustrated by the mean streamwise velocity fields with streamlines superimposed, as shown in Fig. 8. The existence of the bump divides the reversed region into two bubbles in both cases. For instance, as shown in panel (a), the upstream bubble located at the leading edge of the bump is much

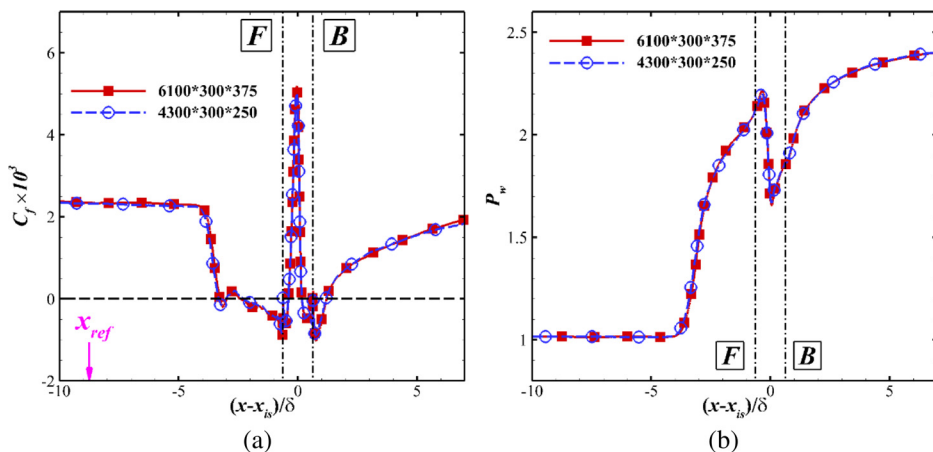


FIG. 5. The comparison of the mean skin friction and surface pressure distributions between two cases: (a) mean skin friction; (b) mean surface pressure. (The dashed black lines represent the bump boundaries, with F and B denoting the front and back edges, respectively.)

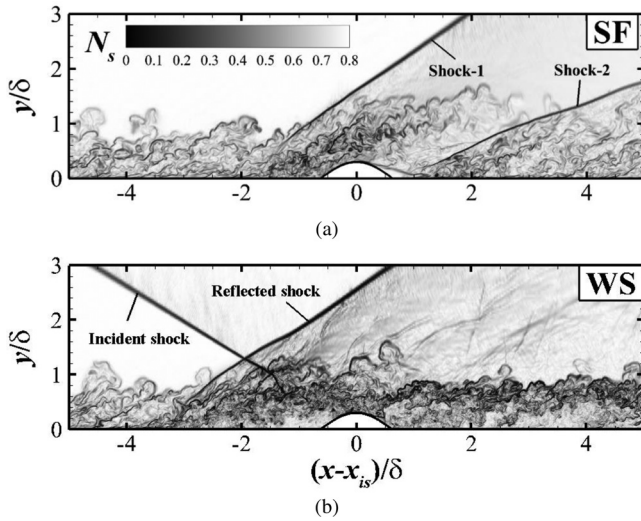


FIG. 6. Instantaneous density gradient flowfield: (a) SF; (b) WS. Lengths are normalized by the boundary layer thickness δ at x_{ref} , and the nominal shock impinging point x_{is} is first subtracted from x .

smaller than the downstream one over the trailing edge of the bump. Both of the described bubbles are enlarged in panel (b), with the upstream separation bubble being more elongated along the streamwise direction, under strong impinging shock effects, which could be considered to drive the separation shock upward. This corresponds to the results presented by Zhang *et al.*,³¹ where an obvious larger separation bubble is observed when the incident shock impinges on the

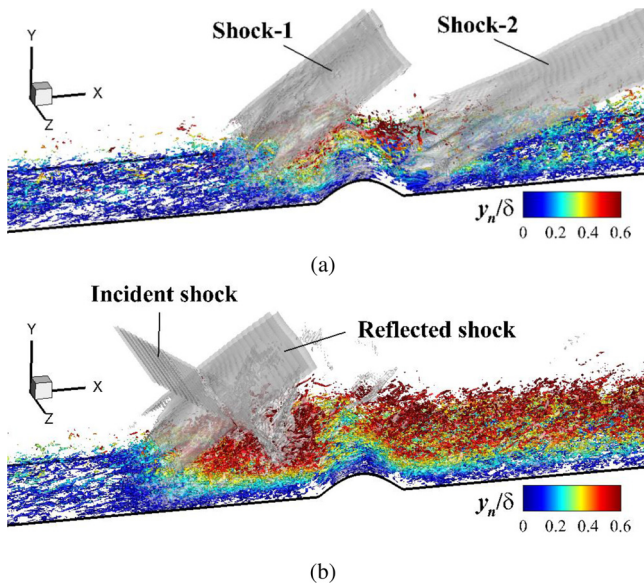


FIG. 7. Iso-surface of $Q=6000$ (approximately 0.9% of the maximum value of Q) follows the Q criterion colored by the wall-normal distance y_n : (a) SF; (b) WS. The shock waves are visualized by iso-surfaces of pressure gradient $|\nabla\rho|\delta/\rho_\infty=80$ and 140 in cases SF and WS, respectively.

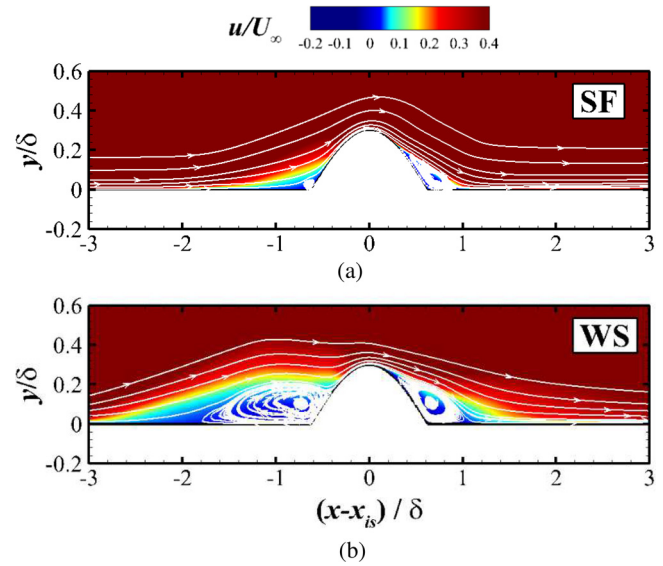


FIG. 8. Mean streamwise velocity field with streamlines in white: (a) SF; (b) WS.

concave surface of the bump windward side, attributed to the pressure rise caused by the bump-induced compression waves and by the incident shock.

The contours of the instantaneous wall skin friction for both cases are shown in Figs. 9(a) and 9(b), respectively, where the streamwise distribution of the mean skin friction is directly compared in Fig. 9(c). The upstream spanwise-alternating streaks are significantly destroyed in the separation region, followed by a recovery in the reattachment region, similar to the results of the previous DNS studies of the reflected interactions. The recovery of the streaks in the case shown in panel (b) is much slower than that in the case shown in panel (a), where no distinct streak structures are observed at $(x-x_{is})/\delta > 2$. This could be related to the enlarged separation bubble located at the trailing edge of the bump [see Fig. 8(b)]. Another notable difference can be seen in the high value for the skin friction at the bump summit in both cases. The extent of the separation region increases, but the peak region is narrower than the case without the incident shock. Quantitative evidence is given in Fig. 9(c), where the peak value ($Cf_{max,WS}=0.005$) in case WS is only 64.34% of that ($Cf_{max,SF}=0.078$) in case SF. The mean separation point, located at $(x-x_{is})/\delta=-1.75$, is moved far upstream to $(x-x_{is})/\delta=-3.31$ by the strong shock interaction. Downstream, rapid growth is captured, followed by a decrease in case SF. A gentle monotonic increase is observed in case WS, which further confirms the slow recovery phenomenon. Streamwise stations x_{ref} and x_{I-x_d} are marked for later analysis of turbulence statistics and the generation mechanism of the skin friction.

B. Unsteady motion of the separation bubbles

To understand the incident shock effects on the unsteady motion of the separation bubbles in the interaction region, Figs. 10(a)–10(d) display instantaneous streamwise velocity fields, with a mean separation bubble edge superimposed; Figs. 10(e) and 10(f) report the time history of the fluctuations of the separation bubble area for both cases.

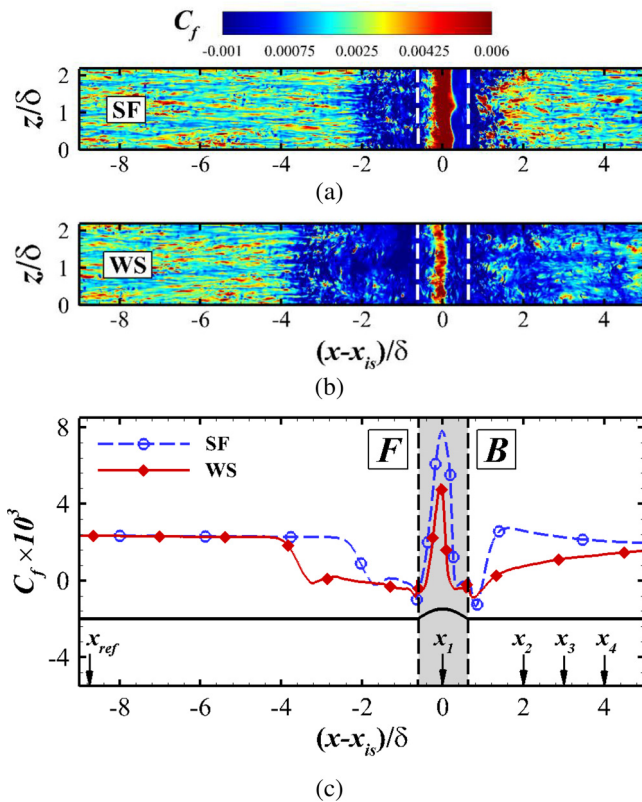


FIG. 9. Contour of the instantaneous skin friction C_f : (a) SF; (b) WS (white dashed lines represent the front and back edges of the bump); (c) the distribution of the mean skin friction C_f (black solid line represents the model surface, and black dashed lines denote the boundaries of the bump).

Typical dilation motions are captured in panels (a) and (b), with a relatively large bubble exceeding the outer edge of the mean bubble in each case, and contraction motions are observed in panels (c) and (d), showing a smaller bubble within the range of the mean bubble. These unsteady motions generally represent the ups and downs of the fluctuating separation bubble area and indicate the constant enlargement and shrinkage of the bubbles, corresponding to the bubble breathing identified in the previous studies of the compression corner interactions¹² and reflected interactions.^{13,33,39} However, the characteristic time scale of the area fluctuation appears to be increased by the shock impingement, approximately from $5U_\infty/\delta$ in case SF to $20U_\infty/\delta$ in case WS, as shown in panels (e) and (f).

The characteristic frequency of the fluctuations of the separation bubble area and the pressure at the mean separation point are quantitatively compared between the two cases in Fig. 11, where the pre-multiplied power spectra density (PSD) is calculated using the Welch method and a Hamming window, with the signal decomposed into four segments with a 50% overlap. The Strouhal number is defined as $st = f\delta/U_\infty$, where f means the frequency, δ is the boundary layer thicknesses, and U_∞ represents the freestream velocity. For the case in panel (a), the dominant frequency $st = 0.12$ in case SF is relatively high, whereas the spectrum of case WS is characterized by low frequencies, attaining a peak value at $st = 0.039$, which is associated with

a time scale of 10–100 times that in the undisturbed turbulent boundary layer, demonstrating the low-frequency features of bubble breathing. For the wall pressure fluctuation at the mean separation point shown in panel (b), the low-frequency peak is found at $st = 0.039$ with the shock impingement, and no considerable low-frequency components are observed without the shock interaction, confirming the low-frequency unsteadiness of shock-induced separation.

To further explore the typical coherent structures in the interaction region, the proper orthogonal decomposition (POD) method is introduced to the instantaneous streamwise velocity field in the middle x - y plane. The POD processed velocity can be written as follows:

$$u(x, y, t) = \overline{u(x, y, t)} + \sum_{k=1}^N a_k(t)\Phi_k(x, y), \quad (2)$$

where the first part of the right side represents the average streamwise velocity, $a_k(t)$ is the time-dependent coefficient of the k th POD mode [represented by the spatial function $\Phi_k(x, y)$], and N is the total number of the POD modes. About 2500 samples are collected within a range of $-4 < (x-x_{is})/\delta < 3$ in the streamwise direction and $-0.1 < y/\delta < 0.5$ in the wall-normal direction. The sampling time step is $\Delta t U_\infty/\delta = 0.1$ so that a total time of $TU_\infty/\delta = 250$ flow time is collected. Based on the described sampling strategy, the maximum frequency can be identified as $st = 5$, with a resolution of $st = 0.004$.

The energy distributions of the POD modes are compared in Fig. 12. The energy of the k th POD mode referred to as E_k is normalized as follows:

$$E_k = \lambda_k / \sum_{m=1}^N \lambda_m, \quad (3)$$

where λ_k is the eigenvalue of the k th POD mode. As shown in Fig. 12(a), the mode energy rapidly drops as the mode number increases, decreasing by about two orders of magnitude from $k = 1$ to $k = 100$. Good agreement with the $k^{(-11/9)}$ law proposed by Mustafa *et al.*⁴⁰ is observed in the intermediate range. Compared with case SF, the mode energy at $k < 10$ in case WS is increased, while a slight decrease is found in the high-order mode at $k > 30$. It is clear that the energy of the first POD mode is increased from 0.052 in case SF to 0.103 in case WS. At $k = 200$, the energy falls from 0.000 818 in case SF to 0.000 683 in case WS. As a result, the first ten POD modes play a leading role in case WS. This behavior is more clearly visualized in Fig. 12(b), where the cumulative energy is shown as a function of the mode number. The first POD mode itself contributes 10.28% and 5.19% in cases WS and SF, respectively. The interaction flowfield is dominated by the low-order modes rather than the high-order modes, which is seen more clearly with the shock impingement. Specifically, the contribution of the first ten POD modes in case WS reaches about 33.1% of the total energy, while these modes in case SF only contribute 24.4%. Moreover, about 68.8% of the total energy is shown in the first 100 modes, while 78.87% is reached with the dedication of the first 200 modes. The first 100 and 200 modes achieve only 62.61% and 73.49% in case SF, respectively. The noticeably lower energy distribution in case SF indicates the much greater importance of the low-order modes in case WS. With the bump introduced in the present simulations, the low-order POD modes still dominate the interaction flow, but the low-frequency motion feature is relatively weakened, which could be

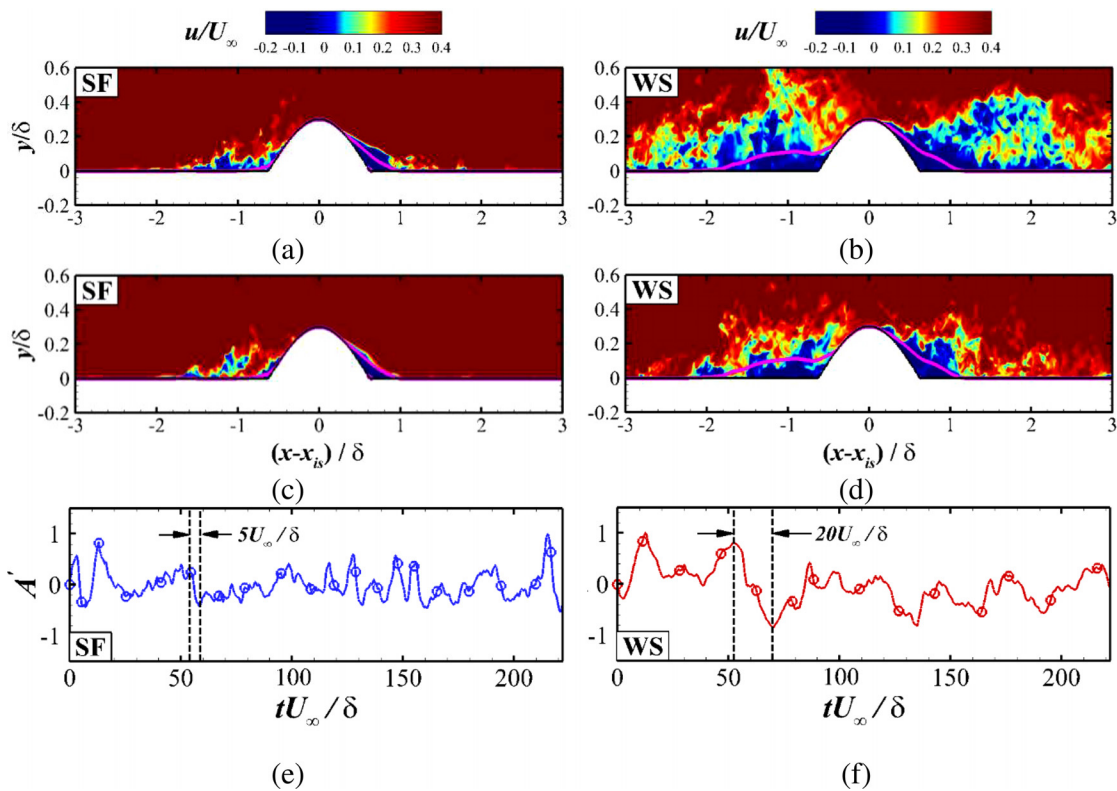


FIG. 10. Unsteady motion of the separation bubbles: the contours of the typical instantaneous streamwise velocity field in cases SF and WS represent dilation motions in [(a) and (b)] and contraction motions in [(c) and (d)]. The pink solid lines indicate the mean separation bubble edge. The time series of the fluctuation of the separation bubble area in cases SF and WS is presented in [(e) and (f)], in which the estimated time scale is marked with black dashed lines and arrows.

quantitatively testified compared with the values of 20.8% and 44.9% contributed by the first and the first ten POD modes obtained by Tong *et al.*³³ in the reflected interaction study on a flat plate under the same flow conditions. In the perspective of flow control, although the separation bubble in the interaction is enlarged by the bump and the incident shock, the low-frequency components are relatively attenuated compared with the bare reflected interactions.

The pre-multiplied PSD of the time coefficient $a_k(t)$ of the POD modes for both cases are shown in Fig. 13. The dominant frequency is rapidly shifted to the high-frequency region when the mode number is increased. The spectra of the modes at $k < 10$ in case WS are different from those in case SF, which are dominated by low frequencies. For example, the peak frequency is concentrated in $st = 0.12$ for case SF and $st = 0.039$ for case WS, consistent with the characteristic

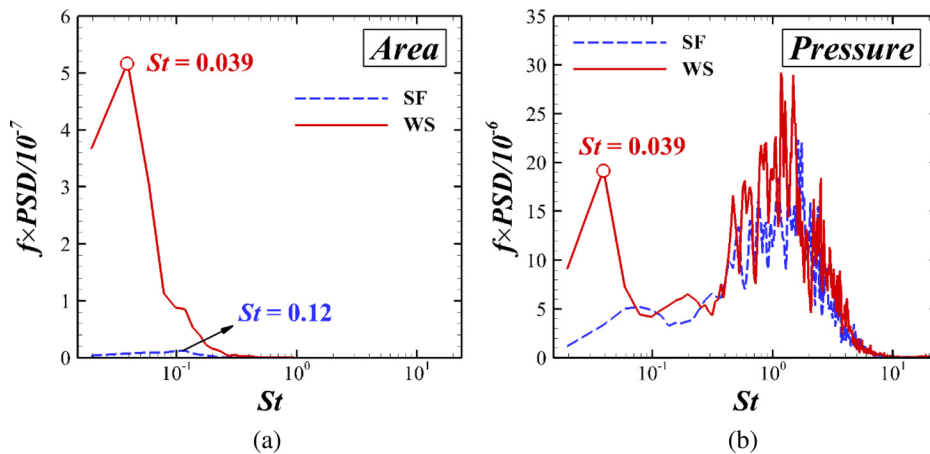


FIG. 11. Pre-multiplied PSD of (a) the separation bubble area fluctuations and (b) the pressure fluctuations at the mean separation point in both cases.

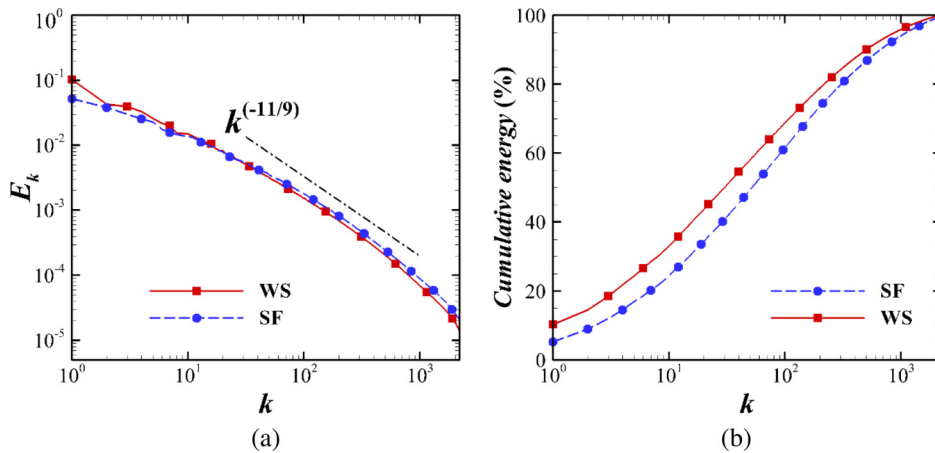


FIG. 12. POD mode energy as a function of the mode number: (a) normalized energy; (b) cumulative energy.

frequencies of the fluctuation of the bubble area. In the high-order modes at $k > 10$, the peak value is decreased, and the peak position moves to the high-frequency region gradually as the mode number increases. As such, the dominance of the low-order modes characterized by the low-frequency flow behaviors is captured again in case WS.

To reveal the relationship between the separation bubble motion and the time-dependent feature of the POD modes, the cross-correlation coefficient C_{MA} is depicted in Fig. 13(c), which is defined as follows:

$$C_{MA}(t) = \frac{\sum_{t=1}^{N_t} A'(t)a'_k(t)}{\sqrt{\sum_{t=1}^{N_t} A'(t)^2 a'_k(t)^2}} \quad (4)$$

with $A'(t)$ and $a'_k(t)$ being the fluctuations of the bubble area and the time coefficient of the POD modes, respectively. The first ten low-

order modes demonstrate a relatively high level of relevance, while the cross-correlation coefficient drops to around zero as the mode number increases. It is reasonable to infer that the unsteady dilation and contraction motions of the separation bubble are closely related to the first ten low-order POD modes, which is particularly striking in the first mode that features the low-frequency unsteadiness in case WS.

The spatial distributions of the five selected modes ($k = 1, 10, 40, 100, \text{ and } 200$) are displayed by the contours of $\Phi_k(x, y)$ for both cases in Fig. 14. The critical structures are generally located between the mean sonic line and the bubble outer edge for both cases in the low-order modes, while no considerable structures can be found in the upstream region. Mode 1 is characterized by two large-scale structures in case SF; one is located at a bump-upstream position, and the other is in the vicinity of the bump rear edge, while only one large-scale structure is observed at the upstream of the bump leading edge in

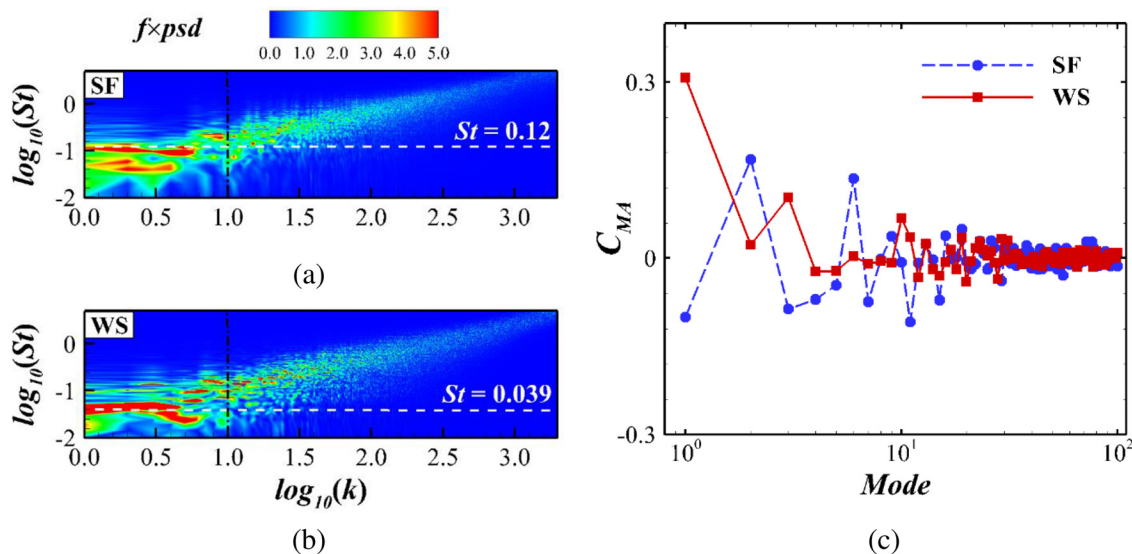


FIG. 13. Unsteady features of the POD mode time coefficient as a function of the mode number: (a) contour of the pre-multiplied PSD in case SF; (b) contour of the pre-multiplied PSD in case WS; (c) cross correlation with the separation bubble area.

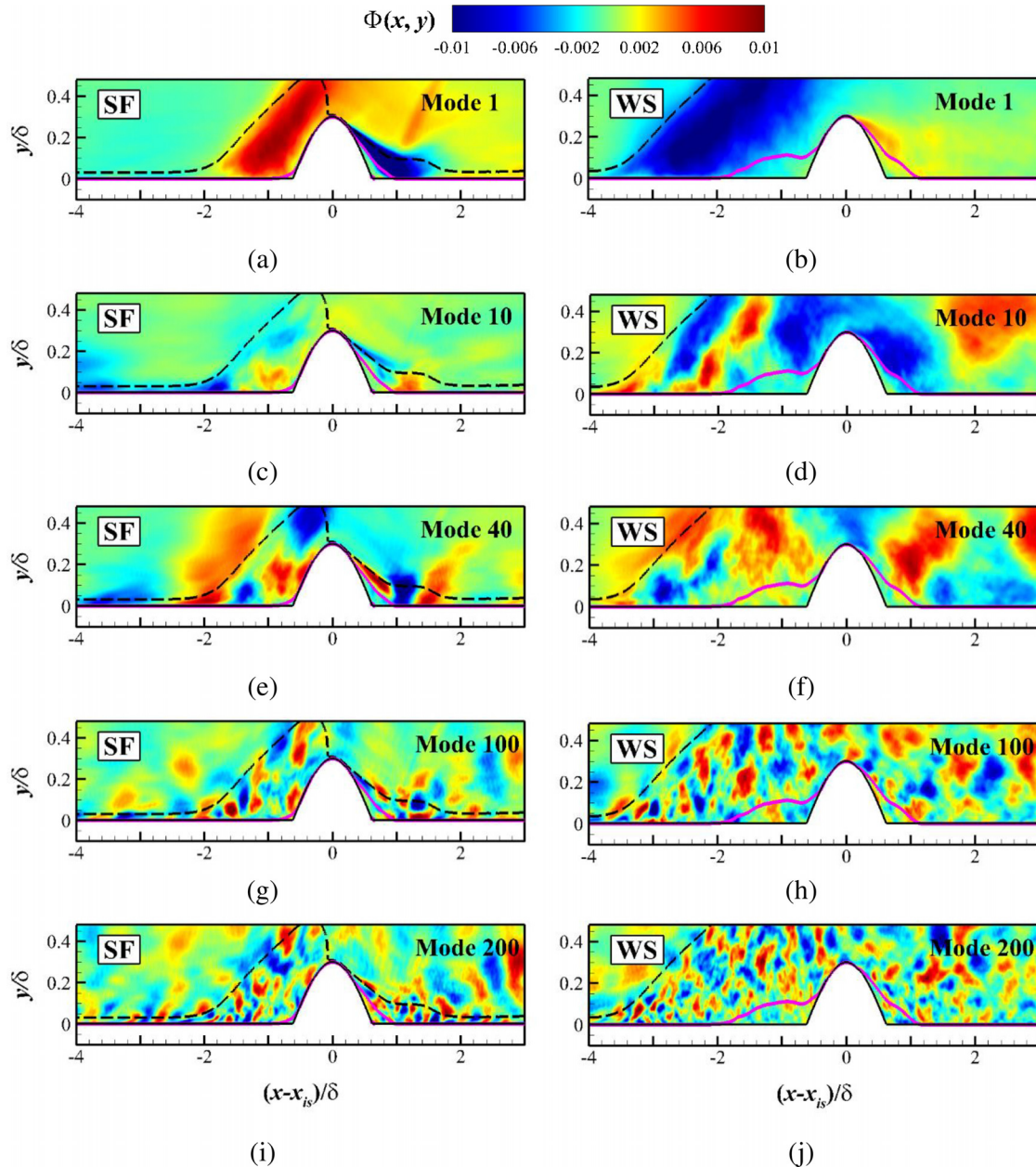


FIG. 14. Spatial distributions of the POD modes with labels in the upper right corner: [(a), (c), (e), (g), and (i)] SF; [(b), (d), (f), (h), and (j)] WS. The dashed black line represents the mean sonic line. The pink solid line denotes the mean separation bubble edge defined by $u = 0$.

case WS. This can be attributed to the strengthened shear layer above the expanded separation bubble, which is associated with the enlarged area of energy concentration upstream of the bump, corresponding to the previous findings on the reflected interactions;⁴¹ it might be related to the inhibition of the flow recompression downstream from the bump. Mode 10 shows a similar distribution to the first mode, but the length scale of energy-containing structures is apparently decreased, probably due to the shedding of the shear-layer vortical structures identified by Dupont *et al.*⁴² As the mode number increases, the

topologies in modes 40, 100, and 200 change dramatically into scenarios dominated by small-scale pieces, which indicate the high-frequency component of the unsteady motions, corresponding to that observed in the shock interactions on a flat plate and over a wavy wall reported by Tong *et al.*^{30,33} It should be noted that, for the high-order modes, the small-scale structures even appear at the upstream side of the sonic line, which is not significantly affected by the shock interaction, as the energy distributions are consistent with those shown in the high-order modes for case SF.

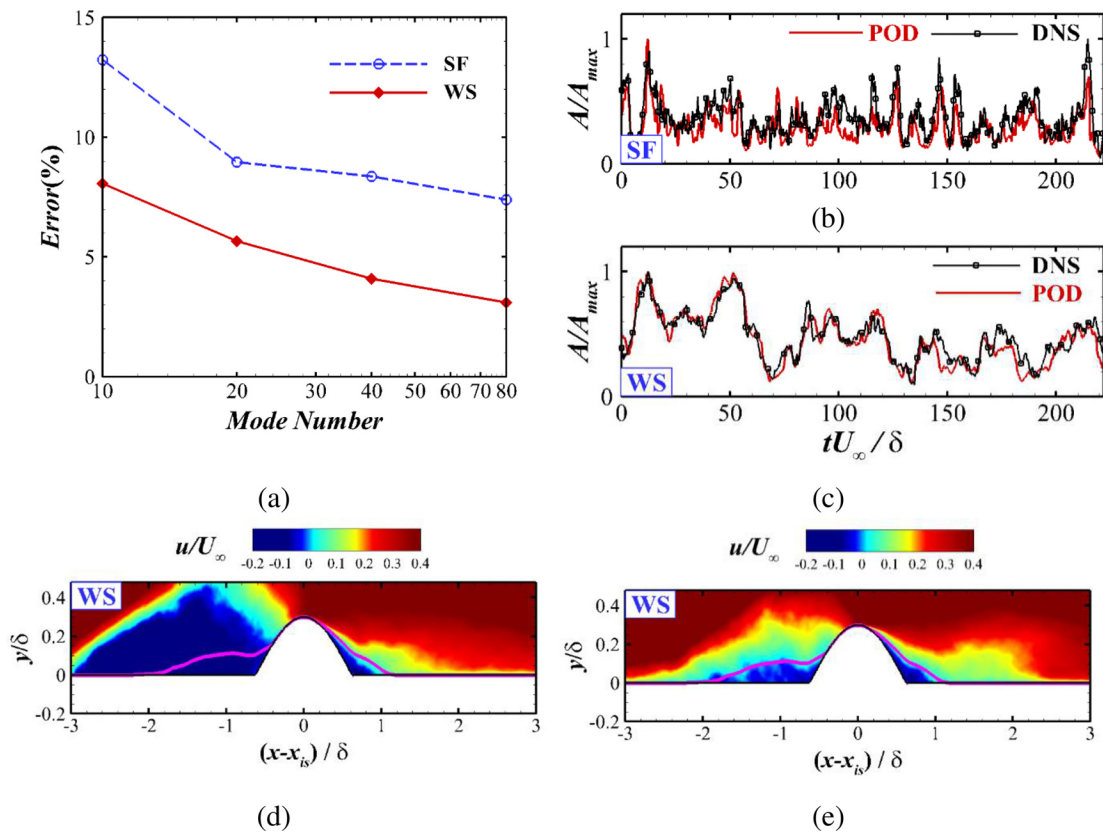


FIG. 15. Reconstructed unsteady motion of the separation bubbles: (a) error in the reconstructed bubble area from the POD modes; original (DNS) and reconstructed (POD) time series of the bubble area fluctuations: (b) SF; (c) WS; contour of streamwise velocity flowfield: (d) dilation motion; (e) contraction motion.

The reconstructed unsteady motion of the separation bubbles from the first ten low-order POD modes is shown in Fig. 15. To evaluate the accuracy of reconstruction, *rms* of the deviation between the bubble area (normalized by its maximum) obtained via DNS is calculated with $\sqrt{\sum_1^N ((A/A_{max})_{POD} - (A/A_{max})_{DNS})^2}$ and compared in panel (a), where the accuracy increases as the number of the POD modes used for reconstruction increases. Compared with case SF, the error based on the first ten modes in case WS is only 8.06%, confirming the satisfactory reconstruction of the affected flowfield. Taking the time history of the bubble area into account, dilation and contraction motions are captured in both cases. However, the low-frequency-dominated bubble motions are well reconstructed in case WS, as the first ten POD modes are characterized by low frequency, and only a portion of the high-frequency features are captured in case SF, due to the absence of the high-order modes that dictate the high-frequency energy. Enlarged and contracted bubbles are reconstructed for case WS in panels (d) and (e), where the streamwise velocity contours display relatively smooth bubble edges as a result of lacking high-frequency components.

C. Turbulence statistics

To gain additional insight into the evolution of the turbulence parameters across the shock interaction region, an analysis of

Reynolds stress components and anisotropy-invariant maps is performed at four selected streamwise stations, denoted by x_1-x_4 , as shown in Fig. 9(c); another three probes, marked as $u_{-1.5}$, d_1 , and d_3 , are placed in the bump upstream region, the bump downstream region, and the reattached boundary layer, respectively, for the TKE analysis. The corresponding results at the upstream reference station x_{ref} are also included for comparison.

The wall-normal profiles of the Reynolds stress components in cases SF and WS are plotted in Figs. 16 and 17, respectively. A general amplification of all of the components is shown in both cases, consistent with the observations of Fang *et al.*¹⁴ and Tong *et al.*³³ in the reflected interactions, with the exception of the suppressed shear component $u''v''$ in the near wall region at the bump summit [see Figs. 16(d) and 17(d)]. It is clear that the overall peak value of each component is increased, with the peak position moving from the near-wall region to an outer layer, supporting the turbulence amplification mechanism due to the free-shear layer or the mixing layer proposed by Wu and Martin,¹⁷ Pirozzoli and Bernardini,⁴³ and Helm *et al.*¹⁸ Taking the streamwise component $u''u''$ as an example, at the bump summit x_1 , the overall peak located at $y_n/\delta = 0.02$ moves outward to $y_n/\delta = 0.25$, where the peak value is 33% higher, while at the downstream stations x_2-x_4 , the peak values intensify by more than 200% and appear at the much further outward position of $y_n/\delta = 0.3-0.4$. Similar phenomena are observed in Figs. 17(b)–17(d) for the

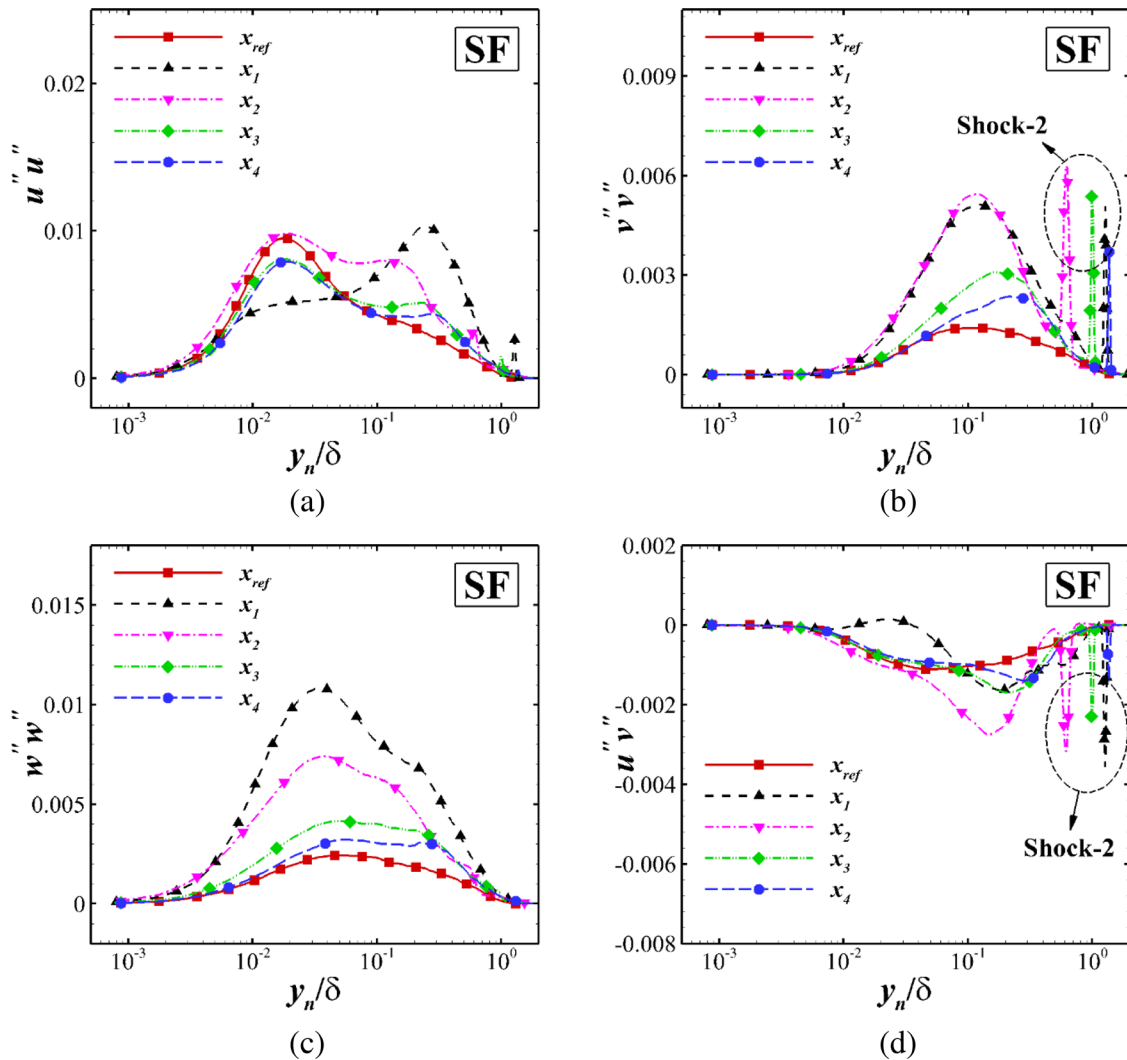


FIG. 16. Wall-normal distribution of the Reynolds stress components at the bump summit x_1 and in the downstream regions along x_2 – x_4 in case SF: (a) $u''u''$; (b) $v''v''$; (c) $w''w''$; (d) $u''v''$.

wall-normal, spanwise, and shear components, respectively, where the shock interactions intensify the peak values by amplification factors of 2–4 relative to case SF, with the peak position being away from the wall at around $y_n/\delta = 0.3$ – 0.4 . Moreover, each component exhibits a tendency to decrease with an outward-moving peak position as the reattached boundary layer develops downstream in both cases, and noticeable differences are apparently preserved in case WS, suggesting a slower recovery that is far from complete.

The Reynolds stress anisotropy-invariant maps at the selected streamwise stations in cases SF and WS are depicted in Fig. 18, where the Reynolds stress anisotropy tensor b_{ij} , the associated second invariant II_b , and the third invariant III_b are written as follows:

$$b_{ij} = \frac{\overline{\rho u_i'' u_j''}}{2\overline{\rho k}} - \frac{1}{3}\delta_{ij}, \quad II_b = b_{ij}b_{ji}, \quad III_b = b_{ij}b_{jk}b_{ki}. \quad (5)$$

Special turbulent states are marked near the vertices and edges of the Lumley triangle⁴⁴ for clarification. At the reference station, it shows a typical anisotropy invariant map of canonical wall turbulence with zero pressure gradient concluded by Pope.⁴⁵ The two-component turbulence due to the blocking effects in the proximity of the wall is well preserved across the interaction region in both cases, with the exception of the state around the downstream reattachment point x_2 in panel (b), which shifts to two-component axisymmetric turbulence due to the effect of the shock impingement, corresponding to the results of Tong *et al.*⁴⁶ for a hypersonic cone/flare model. As the wall-normal distance increases, the maximum anisotropy at each station is attained at around $y/\delta \approx 0.01$ in the buffer layer, which coincides with previous results obtained by Pirozzoli *et al.*,³⁶ although the anisotropic intensity is weakened in the interaction region. However, the comparison between two cases at the bump summit x_1 highlights the most

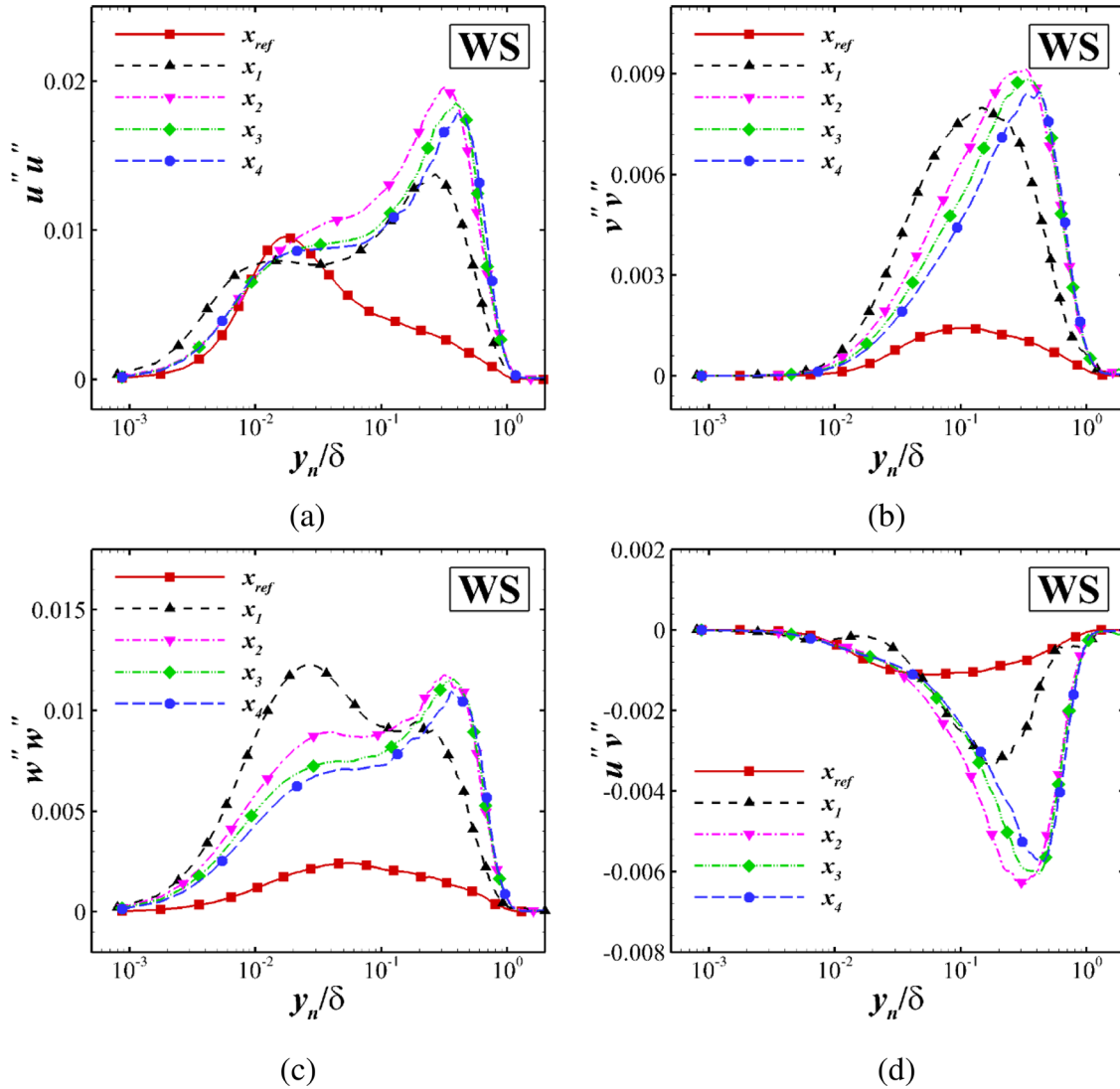


FIG. 17. Wall-normal distribution of the Reynolds stress components at the bump summit x_1 and in the downstream regions along x_2 – x_4 in case WS: (a) $u''u''$; (b) $v''v''$; (c) $w''w''$; (d) $u''v''$.

significant change, where a sharp drop to the axisymmetric compression limit occurs at y/δ highlights the most significant change, where a sharp drop to the axisymmetric compression limit occurs at $y/\delta \approx 0.01$, followed by a reversal toward the axisymmetric expansion limit before approaching a more isotropic turbulence. This phenomenon qualitatively resembles that found in the previous investigations on a compression–expansion ramp by Grilli *et al.*⁴⁷ and a double-compression ramp by Tong *et al.*⁴⁸

Figure 19 displays the contours of the mean TKE defined as follows:

$$k = \overline{\rho u_i u_i} / 2\rho \tag{6}$$

in the interaction region of $-4 < (x-x_{is})/\delta < 3.5$ in the streamwise direction and $0 < y_n/\delta < 1.5$ in the wall-normal direction for cases SF and WS, respectively. As expected, a significant amplification of the

TKE around the bump is observed between the sonic line and the separation bubble line in both cases, with an overall peak value occurring in the separated shear layer associated with the main separation bubble. Specifically, the streamwise range of the amplified TKE region upstream of the bump is increased in length, as a result of the enlarged separation bubble [see Fig. 8(b)]. Note that the amplification factor of the TKE in the downstream region of case WS decreases to 33% of the peak value obtained in panel (a), which is probably related to the loss of the bump-induced shock 2 in case SF. Another notable difference between the two cases is related to the peak TKE position. The overall peak in case SF is located near the wall at $y_n/\delta = 0.08$, while the distance from the wall of the maximum value of the TKE in case WS is more than twice that, which is relevant to the uplifted large-scale vortical structures seen in panel (b), coinciding with the previous

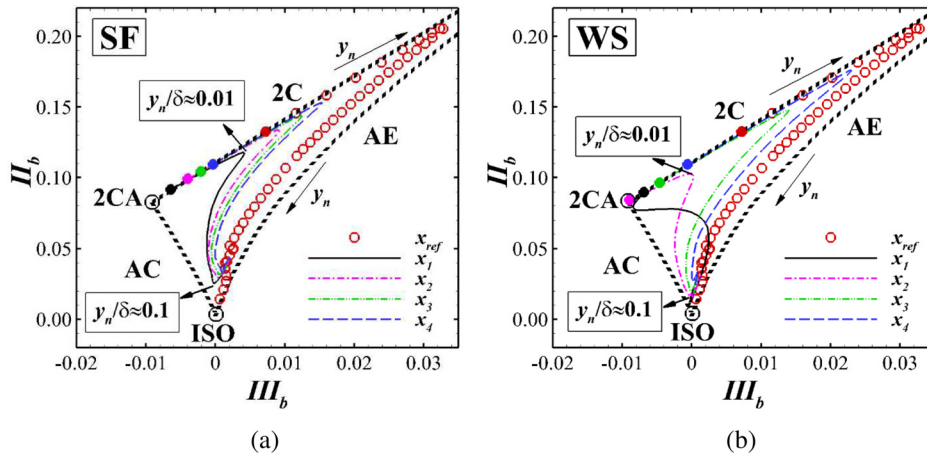


FIG. 18. Anisotropic invariance of the Reynolds stress: (a) SF; (b) WS; (1C: one-component state, 2C: two-component state, AE: axisymmetric expansion state, ISO: isotropic state, AC: axisymmetric compression state, 2CA: two-component axisymmetric state); the top right corner represents the one-component state, which is not presented here. Red circles display the results within $y_n/\delta = 1$ at the reference station x_{ref} .

observations by Sun *et al.*⁴⁹ of a supersonic turbulent boundary over a concave surface at a similar Reynolds number based on the momentum thickness of $Re_\theta \approx 3600$.

Figure 20 shows the wall-normal profiles of the mean TKE along the various streamwise stations for both cases. Similar to the asymptotic behavior of the TKE in the near-wall region in incompressible boundary layers found by Patel *et al.*⁵⁰ and Speziale *et al.*,⁵¹ Pirozzoli and Grasso³⁵ reported the varying density-scaled TKE k^+ as a function of the wall-normal distance y_n^+ in a compressible flow, with the definition of k^+ and its relation with y_n^+ written as follows:

$$k^+ = \bar{\rho}k / (\bar{\rho}_w u_\tau^2), \quad k^+ = A^+ y_n^{+2}, \quad (7)$$

where $\bar{\rho}$ refers to the average density, subscript w denotes the variable at the wall, u_τ is the friction velocity, and A^+ is a constant. At x_{ref} , k^+

strictly obeys the asymptotic relation with a constant of $A^+ = 0.10$ in the near-wall region. The peak reaches $k^+ = 4.43$ at $y_n^+ = 13.82$, which is comparable with $k^+ = 5.25$ at $y_n^+ = 14.3$ obtained by Pirozzoli and Grasso,³⁵ which is consistent with the $k^+ = 4.50$ at $y_n^+ = 15$ reported by Patel *et al.*⁵⁰ in the incompressible case. The constant A^+ increases across the interaction region, and it drops and approaches the reference value as the reattached boundary layer develops downstream in both cases. Recalling the contours in Fig. 19(a), the TKE is dramatically altered near the wall, so that the TKE profiles are greatly augmented, and a platform is formed in the inner region seen in Fig. 20(a). For instance, the peak at station d_1 is attained at $y_n^+ = 42$ with an amplification factor of 5.7, influenced by the bump-induced shock 2 interaction. By contrast, as shown in Fig. 20(b), an outer peak of station $u_{-1.5}$ is found at $y_n^+ = 307$, where k^+ is intensified to 3.1 times the reference value, which could be attributed to the large-scale vortical structures. It was noted by Smits *et al.*⁵² that very-large-scale motions dominate the TKE production in the outer layer for the high Reynolds number flows. After passing through the interaction region, there is a rapid collapse near the wall, while a slight deviation from the upstream profile in the outer region is observed; a slower returning tendency in the outer region is seen in panel (b), associated with an enlarged downstream separation bubble and the corresponding gentle recovery of the separated shear layer.

The TKE budget could be briefly described as follows:

$$\frac{\partial \bar{\rho}k}{\partial t} = C + T + P + V + K + M - D, \quad (8)$$

where $C, T, P, V, K, M,$ and D denote the convection, turbulence transport, production, viscous diffusion, pressure-dilation correlation, acceleration, and viscous dissipation terms, respectively. More details for each term can be found in Adumitroaie *et al.*⁵³ The TKE budget at the selected streamwise stations is presented in Fig. 21 for both cases. In the upstream turbulent flow, the transportation of the TKE is concentrated in the inner layer, with continuously turbulent production and dissipation, which is balanced by viscous diffusion and turbulence transport. The convection term and the direct effects of compressibility are negligible, indicating a typical TKE budget, coinciding with the findings of Pirozzoli *et al.*³⁶ However, transportation is extended to a much further outward position in the affected region; for example, at

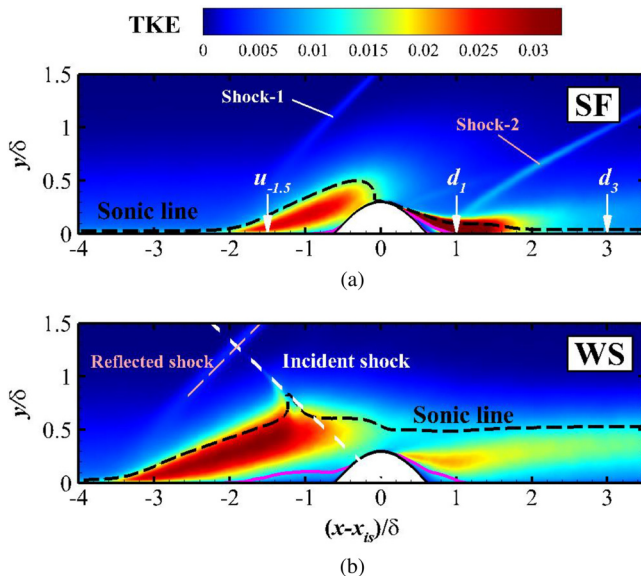


FIG. 19. Contours of the mean TKE: (a) SF; (b) WS. Dashed line in black represents the mean sonic line. The pink solid line denotes the mean separation bubble edge defined by $u = 0$.

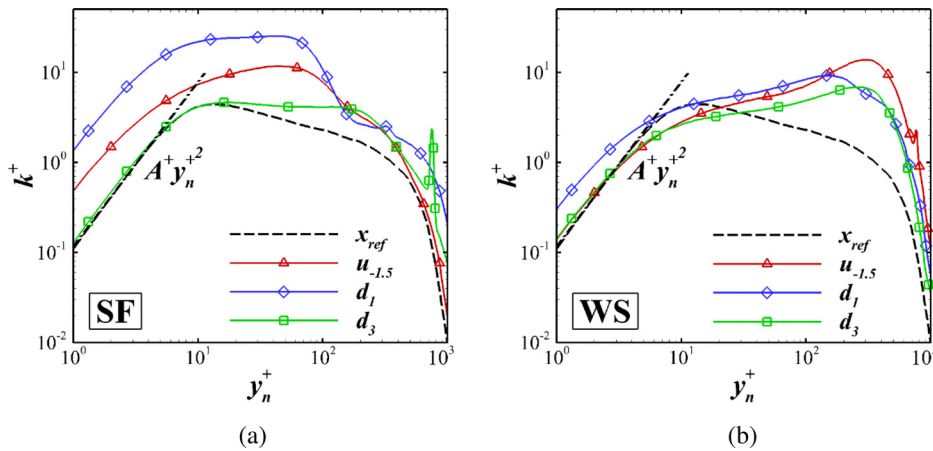


FIG. 20. Mean TKE profiles along the various streamwise stations: (a) SF; (b) WS. Three specific streamwise stations are given: station $u_{-1.5}$ [$(x-x_{is})/\delta = -1.5$] in the upstream region is associated with the peak TKE in case WS, while station d_1 [$(x-x_{is})/\delta = 1$] stands in the downstream region, where the peak TKE occurs in case SF; station d_3 [$(x-x_{is})/\delta = 3$] is in the recovery boundary layer.

$u_{-1.5}$, the original peak position of turbulence production moves from $y_n/\delta \approx 0.01$ to $y_n/\delta \approx 0.1$ in case SF, which further moves to $y_n/\delta \approx 0.4$ in case WS. In the outer layer, the affected transportation of the TKE largely depends on the turbulence transport and dissipation to consume the turbulence produced, as the viscosity is barely diffused in this region. Another interesting finding is identified in the convection term, which balances the flow in the outer layer. At the downstream station d_3 , a complete return to the original state in the near-wall region can be observed with a slight discrepancy in the outer region compared with the undisturbed TBL [Fig. 21(f)]. The outward positioned transportation region in panel (g) implies an obviously unfinished recovery process, confirming the finding shown in Fig. 20.

D. Decomposition of the mean skin friction

The mean skin friction coefficient denoted as C_f is, in fact, the ratio of mean wall shear stress τ_w to the dynamic pressure of the free-stream. The definition is

$$C_f = \tau_w / \left(\frac{1}{2} \rho_\infty U_\infty^2 \right), \tag{9}$$

where ρ_∞ and U_∞ are the freestream density and velocity, respectively. Based on the skin friction decomposition idea proposed by Fukagata *et al.*⁵⁴ for the incompressible flows, Li *et al.*⁵⁵ derived the decomposition expression extended to the compressible flows following the Renard–Deck identity⁵⁶ by manipulating several coordinate transformations and integrals in the momentum equation. The same idea of the decomposition is also used to explore the heat flux generation mechanism on a hypersonic flat plate by Sun *et al.*⁵⁷ Therefore, from an energy perspective, the skin friction coefficient can be decomposed as follows:

$$C_f = C_{f,V} + C_{f,T} + C_{f,G}, \tag{10}$$

where $C_{f,V}$ is interpreted as the direct viscous dissipation. $C_{f,T}$ denotes the power spent for the TKE production. $C_{f,G}$ is related to the spatial growth. More specifically, the physically informed contribution terms in Eq. (10) can be explicitly expressed as follows:

$$C_{f,V} = \frac{2}{\rho_\infty U_\infty^3} \int_0^\infty \bar{\tau}_{yx} \frac{\partial \tilde{u}}{\partial y} dy,$$

$$C_{f,T} = \frac{2}{\rho_\infty U_\infty^3} \int_0^\infty \bar{\rho} (-u''v'') \frac{\partial \tilde{u}}{\partial y} dy,$$

$$C_{f,G} = \frac{2}{\rho_\infty U_\infty^3} \int_0^\infty (\tilde{u} - U_\infty) \times \left[\bar{\rho} \left(\tilde{u} \frac{\partial \tilde{u}}{\partial x} + \tilde{v} \frac{\partial \tilde{u}}{\partial y} \right) + \frac{\partial}{\partial x} (\bar{\rho} u''u'' - \bar{\tau}_{xx}) + \frac{\partial \bar{P}}{\partial x} \right] dy, \tag{11}$$

where τ_{xy} and τ_{xx} are shear stress and normal stress, respectively. A detailed derivation of Eq. (11) is available in Li *et al.*⁵⁵

Taking the differences in the streamwise distribution of C_f between the two cases shown in Fig. 9(c), the shock interaction effects on the generation mechanism of the mean skin friction are evaluated by means of the decomposition technology. The fractional contribution of the terms in Eq. (10) to the overall mean skin friction at the reference station x_{ref} and four streamwise stations denoted as x_f-x_4 are listed in Fig. 22. The decomposition results are accurate and reliable within an acceptable relative error, defined as $(C_{f,V} + C_{f,T} + C_{f,G} - C_f)/C_f$ and confined within $\pm 2\%$ at all of the considered stations. In accordance with the results in the upstream TBL presented by Fan *et al.*⁵⁸ on a zero-pressure-gradient TBL, all of the three decomposed terms show positive contributions to the overall skin friction at x_{ref} . Specifically, the fractional contributions $C_{f,V}/C_f$, $C_{f,T}/C_f$ and $C_{f,G}/C_f$ are 40.47%, 46.15%, and 13.35%, respectively, confirming the important role of $C_{f,V}$ and $C_{f,T}$, which is consistent with the data proposed by Tong *et al.*⁵⁹ in the study of the reflected interactions. This also quantitatively corresponds to the decomposition results in the upstream TBL before an expansion corner presented by Zhang *et al.*⁶⁰

As reported in Fig. 22(a), the contribution of each term remains positive at the bump summit x_f . However, two notable differences should be pointed out. First, the generation of the skin friction is determined by one specific dominant contributor, with the contribution exceeding 50% in both cases. Second, the leading role of $C_{f,G}$ in case SF is taken over by $C_{f,T}$ with the shock interaction. More specifically, $C_{f,T}$ produces 60.49% of the overall C_f in case WS, which implies that the skin friction depends on the spent power for the TKE production. By contrast, the magnitude of the contribution from $C_{f,G}$ is 50.26% in case SF, which could be related to the significant pressure gradient in the vicinity of the bump summit. According to the location of the mean

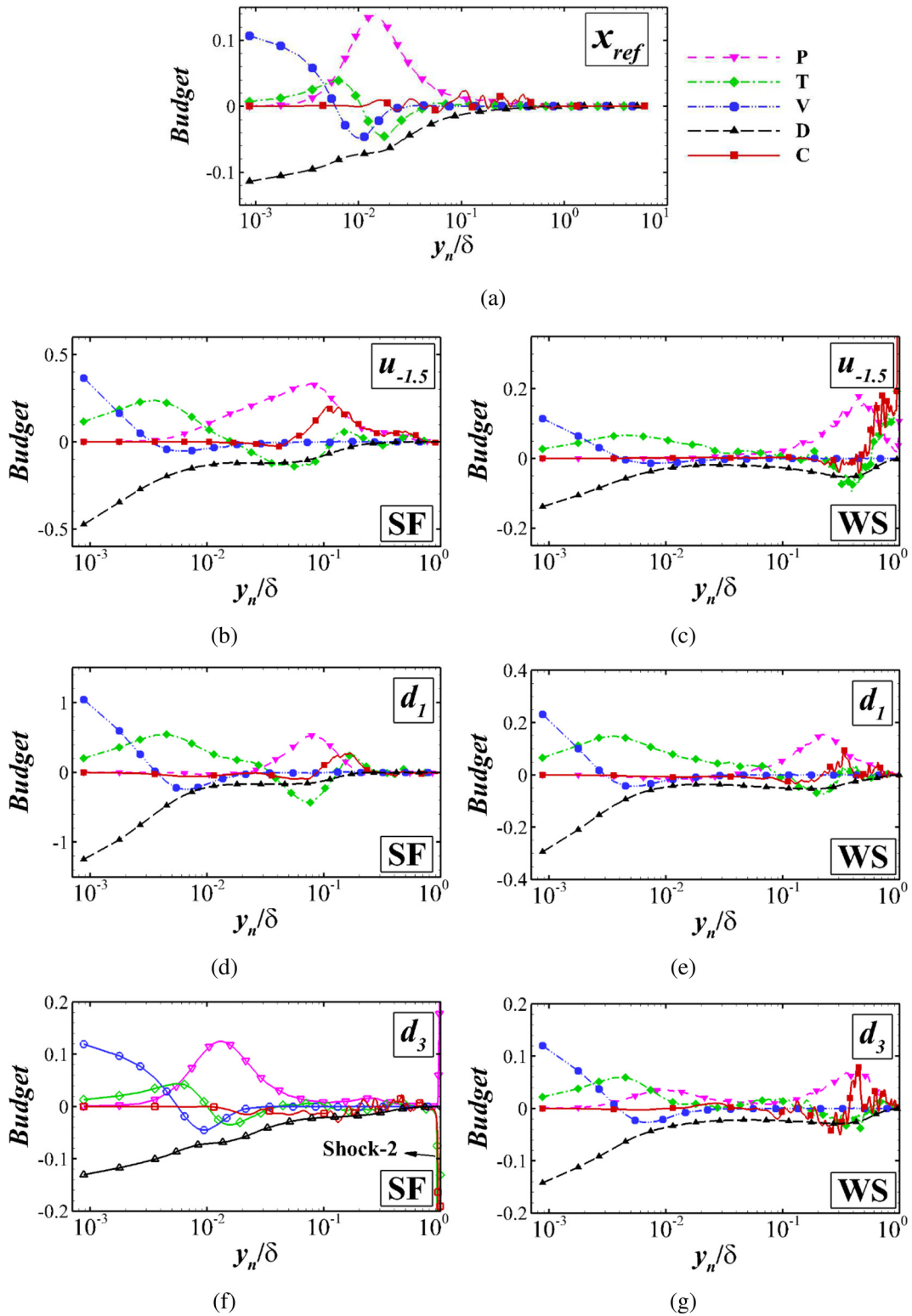


FIG. 21. Wall-normal distribution of the TKE budget along the streamwise stations at: (a) x_{ref} ; [(b) and (c)] $u_{-1.5}$; [(d) and (e)] d_1 ; [(f) and (g)] d_3 (D: viscous dissipation term; P: TKE production term; T: turbulence transport term; V: viscous diffusion term; C: convection term).

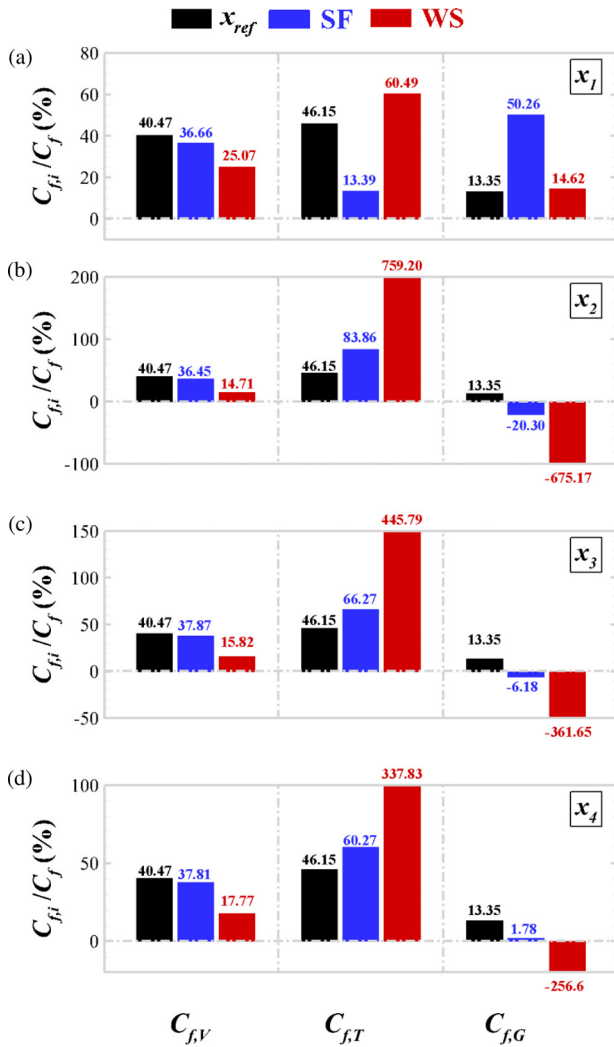


FIG. 22. Contributions to the wall skin friction at streamwise locations: (a) x_1 [$(x-x_{is})/\delta = 0$]; (b) x_2 [$(x-x_{is})/\delta = 2$]; (c) x_3 [$(x-x_{is})/\delta = 3$]; (d) x_4 [$(x-x_{is})/\delta = 4$]. [The relative position of the selected streamwise locations are marked in Fig. 9(c).]

sonic line in Fig. 18, the spatial development associated with the separated shear layer exhibits different behaviors above the bump, which may be the reason for the altered $C_{f,G}$.

Obvious changes downstream of the bump trailing edge should be emphasized [Figs. 22(b)–22(d)]. In both cases, the generation of C_f is dominated by a very large positive $C_{f,T}$, which is counterbalanced by a large negative $C_{f,G}$, corresponding to the characteristics observed by Fan *et al.*⁵⁸ and Tong *et al.*⁵⁹ Taking the decomposition results at station x_2 as an example [Fig. 22(b)], the contribution of $C_{f,T}$ is drastically increased to 759.20%, and 88.93% of the contribution is canceled out by $C_{f,G}$. $C_{f,T}$ and $C_{f,G}$ clearly exhibit a gradually decreasing fractional contribution from x_2 to x_4 . As in case WS, the contribution of $C_{f,T}$ at x_4 is reduced to half of the magnitude at x_2 . The absolute value of the contribution made by $C_{f,G}$ decreases from 675.17% at x_2 to 256.6% at x_4 . It should be noted that, in Fig. 22(d), $C_{f,G}$ returns to make a positive contribution in the reattached boundary layer at x_4 , which is a sign of

the rapid recovery from the bump effects. However, the recovery is suppressed by the incident shock interaction and is far from complete. In addition, $C_{f,V}$ is nearly unchanged as a moderate contributor to the skin friction generation in case SF, while it remains rather small and negligible in case WS.

Due to the decisive importance of the power spent on the TKE production term, the characteristic length scale of the fluctuations subjected to $C_{f,T}$ deserves further investigation. To extract the contribution of the different scales of turbulent motions, multi-scale interactions in a compressible boundary layer are discussed by Agostini *et al.*⁶¹ through empirical mode decomposition (EMD). In this way, a bidimensional EMD method is applied in the turbulent channel flows to identify the scales of attached eddies, following Cheng *et al.*⁶² The velocity fluctuations are split into several scale-featured components, allowing the quantification of the contribution to the skin friction associated with the Reynolds stress. Another scale decomposition method, which is, in fact, a spectral analysis and different from a bidimensional EMD, is proposed by Duan *et al.*⁶³ to further clarify the contributions of various scales to the skin friction generation following FIK identity in the channel flows. Likewise, this idea could be employed on the Renard–Deck identity decomposition method. The cospectra of the Reynolds shear stress at a given y location are calculated as follows:

$$\Phi_{u''v''}(k_z) = c \overline{\text{Real}[\tilde{u}(k_z)\tilde{v}^*(k_z)]}, \quad (12)$$

where k_z is the spanwise wave number, the upper tilde refers to the Fourier transform, and *Real* indicates the real part of a complex. The asterisk denotes the complex conjugate, and c is a constant determined by

$$\widetilde{u''v''} = \int_0^\infty \Phi_{u''v''}(k_z) dk_z. \quad (13)$$

If we denote the integrand F_{RD} in $C_{f,T}$ as

$$F_{RD} = -2\bar{\rho} \widetilde{u''v''} \frac{\partial \tilde{u}}{\partial y}, \quad C_{f,T} = \int_0^\infty F_{RD} dy \quad (14)$$

then the spectra of F_{RD} can be written as

$$\Phi_{F_{RD}}(k_z) = -2\bar{\rho} \frac{\partial \tilde{u}}{\partial y} \Phi_{u''v''}(k_z), \quad F_{RD} = \int_0^\infty \Phi_{F_{RD}}(k_z) dk_z. \quad (15)$$

Because the spectra of $C_{f,T}$ are

$$\Phi_{C_{f,T}}(k_z) = \int_0^\infty \Phi_{F_{RD}}(k_z) dy. \quad (16)$$

$C_{f,T}$ is given by

$$\begin{aligned} C_{f,T} &= \int_0^\infty \int_0^\infty \Phi_{F_{RD}}(k_z) dk_z dy = \int_0^\infty \int_0^\infty \Phi_{F_{RD}}(k_z) dy dk_z \\ &= \int_0^\infty \Phi_{C_{f,T}}(k_z) dk_z. \end{aligned} \quad (17)$$

Finally, the contribution of $C_{f,T}$ can be expressed as follows:

$$\frac{C_{f,T}}{C_f} = \int_{-\infty}^\infty \int_{-\infty}^\infty \frac{k_z y \Phi_{F_{RD}}(k_z)}{C_f} d(\ln(k_z)) d(\ln y). \quad (18)$$

From Eq. (17), this can be rewritten as follows:

$$\frac{C_{f,T}}{C_f} = \int_0^\infty \frac{k_z \Phi_{C_{f,T}}(k_z)}{C_f} d(\ln(k_z)). \quad (19)$$

Therefore, the local contribution of a specific length scale at a given y position to C_f can be read from a contour in the (λ_z, y) plane with logarithmic scales based on Eq. (18). In addition, the integration over all y positions makes it possible to assess the contribution of one specific scale or a range of specific scales to $C_{f,T}$ by plotting the integrand as a function of the spanwise wavelength in logarithmic scale following Eq. (19).

To visualize and detail the described scale analysis, Fig. 23 exhibits the local-scale contribution in inner-scale units of the TKE production at the reference station x_{ref} . First, the peak shown in panel (a) appears very near to the wall at $y_n^+ = 14$, with a length scale of $\lambda_z^+ = 82$, revealing the predominance of small-scale structures. Using Eq. (19), the contribution of the fluctuations with specific length scales can be read from panel (b), where the total contribution of the TKE production to C_f is represented by the total area below the curve. As contributions at any range of λ_z^+ can be extracted from a line graph, we choose $\lambda_z^+ = 200$ as the threshold to distinguish between small-scale and large-scale structures, labeled zone I and zone II in this figure. Quantitatively, contributions at certain scales possess 62.64% in zone I and 37.36% in zone II, which agrees well with that found in the upstream TBL of the reflected interactions conducted by Tong *et al.*⁵⁹ They adopted the bidimensional EMD method to split the velocity fluctuations into four modes and defined the first two modes as small-scale structures and the third and fourth as large-scale structures. About 60% of the contribution from modes 1 and 2 to $C_{f,T}$ is given in their work, which is comparable with the contribution of the small-scale part in the present study. Cheng *et al.*⁶² pointed out that the low-order EMD modes with $\lambda_z^+ = 100\text{--}200$ are related to near-wall streaks and quasi-streamwise vortices in the turbulent channel flows, and

Tong *et al.*⁵⁹ observed similar near-wall small-scale structures concentrating $\lambda_z^+ \approx 100$ in the reflected interactions, which contribute most to the TKE production term. It should be noted that no specific value of λ_z^+ can be identified as distinguishing the different scales in bidimensional EMD. The same conclusion regarding a small-scale-dominated feature is obtained as in the previous studies, although two different methods are adopted. Therefore, the selected threshold is reasonable for the present study. We must emphasize again that the contribution of any specific physical length scales to the skin friction can freely be supplied using this scale decomposition method.

To estimate the shock interaction effects on the C_f generation mechanism, the scale- and position-dependent contributions of $C_{f,T}$ at the reattached boundary layer at the downstream station x_4 are reported for cases SF and WS in Figs. 23 and 24, respectively. In Fig. 24(a), two peaks are presented at the scale-decomposed spectral contour. A short-wavelength peak is found at $y_n^+ = 15$ in the near wall region, with a small scale of $\lambda_z^+ = 97$. A long-wavelength peak appears at $y_n^+ = 241$, which is much further from the wall in the outer region, associated with the wavelength of $\lambda_z^+ = 414$. However, as shown in panel (c), only one outer peak is observed with the incident shock interaction. At the peak location of $y_n^+ = 389$, the associated spanwise wavelength of $\lambda_z^+ = 552$ implies a much larger structure than that in case SF. As seen in panel (d), the contribution of the large-scale fluctuations is much larger than that of the small-scale structures, as the curve is much closer to the zero line in the short-wavelength range. The leading role of the large-scale structures in case WS might be related to the enlarged vortical structures downstream of the shock interaction.

Figure 25 quantitatively compares the contribution of the small-scale and large-scale fluctuations before and after the shock interaction in both cases. The contributions of zone I and zone II obtained in Fig. 23(b) at x_{ref} is also included in Fig. 25(a) for comparison. The large-scale contribution in the basic bump flow increases by 12.36% with respect to that in the upstream TBL at x_{ref} . The percentage in zone I is

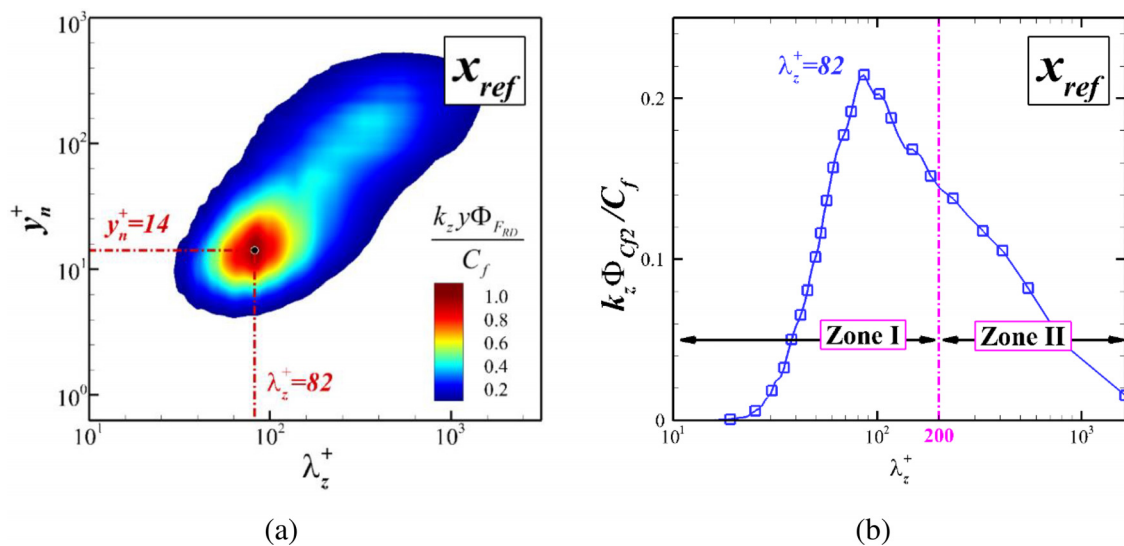


FIG. 23. Scale decomposition results at location x_{ref} . (a) spectral contour; (b) contribution of the physical length scale to the mean skin friction (text in pink boxes: zone I covers the region of $\lambda_z^+ \leq 200$, otherwise, assign λ_z^+ to zone II).

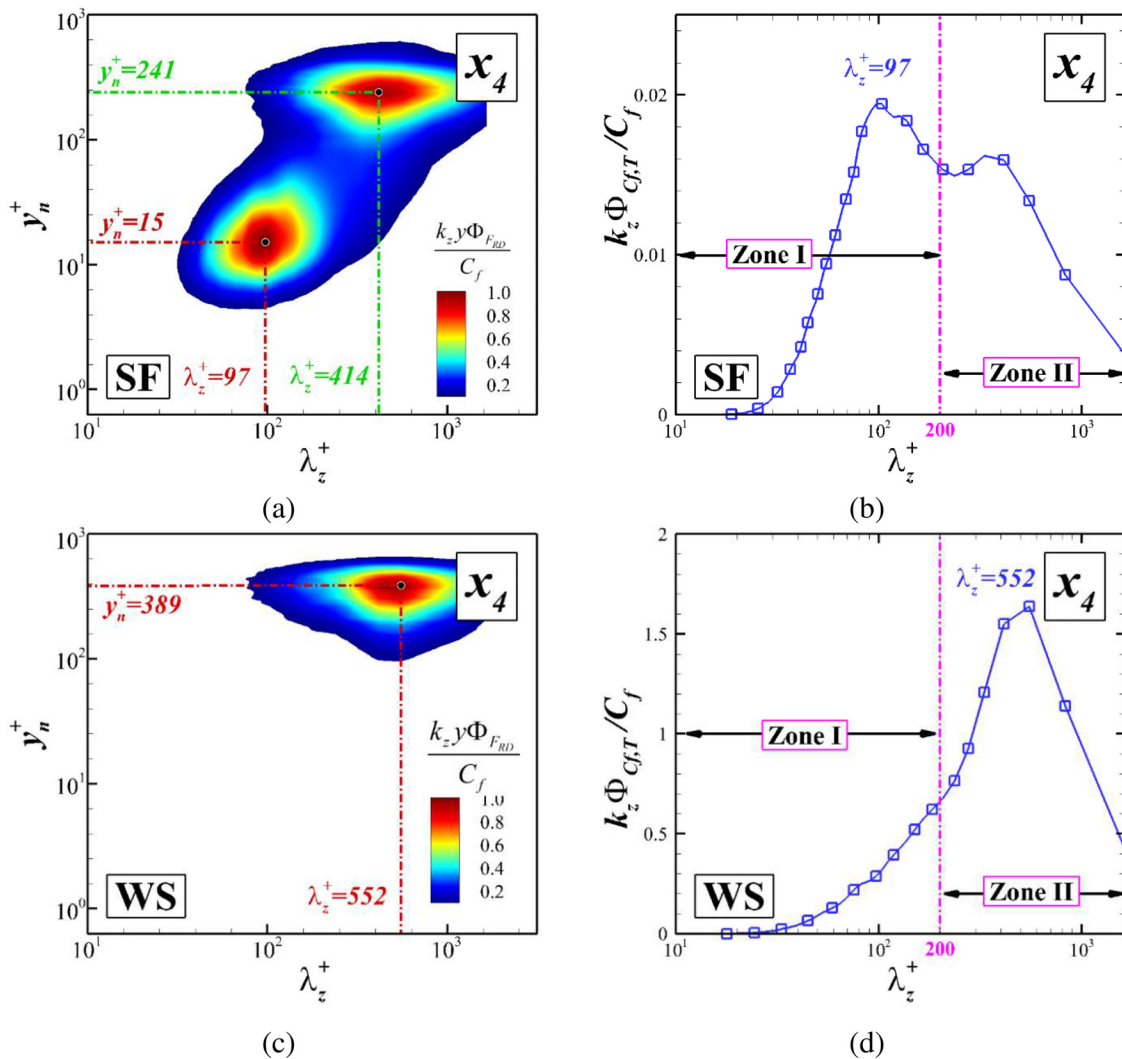


FIG. 24. Scale decomposition results at location x_4 : (a) spectral contour for case SF; (b) contribution of the physical length scale to the mean skin friction; (c) spectral contour for case WS; (d) contribution of the physical length scale to the mean skin friction.

only 0.56% higher than that in zone II [Fig. 25(b)], suggesting that the large-scale and small-scale fluctuations are almost equally important for the TKE production. However, the contribution of the large-scale fluctuations are greatly enhanced [Fig. 25(c)], which coincides with the results reported by Tong *et al.*⁵⁹ that large-scale structures in logarithmic and outer regions have the advantage of controlling the TKE production in the reattached boundary layer. To be specific, they found the large-scale energy-containing structures with $\lambda_z^+ = 316\text{--}1000$ in the reflected interactions, contributing more than 67% of the TKE production term, which might be associated with larger streaks and vortex packets in the outer layer, as presented by Cheng *et al.*⁶² through the EMD analysis of the velocity fluctuations in the turbulent channel flows. In the present study, due to the shock interaction, the contribution of the small-scale structures is greatly suppressed, and the contribution of the large-scale structures is

increased to 80.80%. Evidently, the contribution of the large-scale fluctuations to the skin friction generation shows an overwhelming significance in the SWBLI flowfield, which should be the priority in efficiently developing the skin friction control technologies.

IV. CONCLUSIONS

The supersonic turbulent flows at $M_\infty = 2.25$ and $Re_\theta \approx 3500$ over a bump with the shock impingement at an angle of 33.2° was investigated and compared with a basic bump flow under the same inflow conditions through the use of DNS. Blowing and suction disturbances were enforced on the wall in the upstream region, and a fully developed turbulent boundary layer was validated by comparing the velocity profiles and turbulence intensities with the previous numerical and experimental results. The responses of unsteady flow separation, turbulence statistics, and skin friction generation to the effects of shock impingement were evaluated.

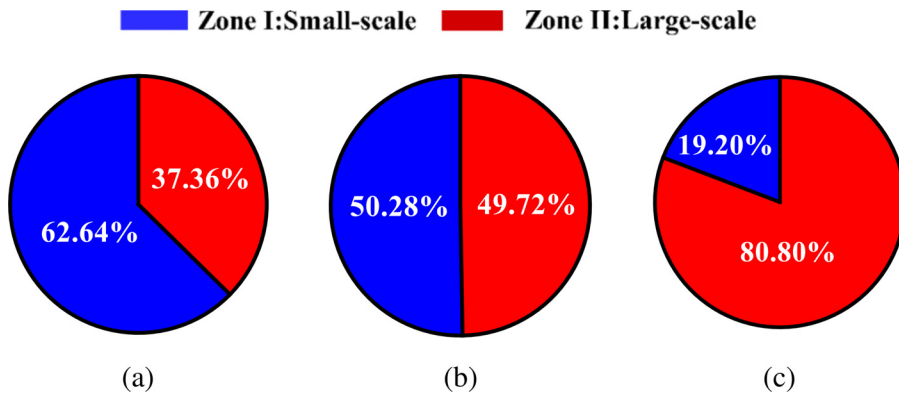


FIG. 25. Contributions of small-scale zone I and large-scale zone II to the TKE production term $C_{f,T}$ at (a) x_{ref} ; (b) and (c) x_4 in cases SF and WS, respectively.

The shock system was qualitatively modified by the shock interaction, such that the downstream shock was completely suppressed, and the upstream separation shock was moved significantly upward. The separation bubbles were found before and after the bump in both cases, and they were greatly enlarged due to the shock interaction, particularly near the leading edge of the bump, where the position of the mean separation point was moved from $(x-x_{is})/\delta = -1.75$ to -3.31 . Abundant vortex structures were lifted away from the wall to the outer layer after they passed through the shock wave, and these were well preserved to the downstream region, as demonstrated by the augmentation of Q vortices. The delayed regeneration of the skin friction streaks, combined with a gently monotonic increase in the mean skin friction, implied a slow recovery from the shock interaction, associated with an enlarged separation bubble and a corresponding shear layer near the trailing edge of the bump.

A spectral analysis of the separation bubble area fluctuations revealed a high-frequency signature in case SF and a low characteristic frequency of $st = 0.039$ in case WS. The corresponding time scale was 10–100 times that of the upstream turbulent boundary layer, suggesting a low-frequency feature of bubble breathing with the shock interaction. The POD analysis of the interaction region showed that the motion of the separation bubble was characterized by the low-frequency unsteadiness and was subjected to the large-scale energy-containing structures from the low-order modes. The reconstruction of the streamwise velocity field in the interaction region from the first ten low-order POD modes partly captured the variation in the high-frequency bubble area in case SF, as the high-order modes were not included here, whereas the reconstructed bubble area time series in case WS showed significant agreement with the original DNS data, and the contraction and dilation motions of the separation bubble were well captured.

General amplification was found in the turbulence parameters, including the Reynolds stress components and the TKE distribution. The profiles of the Reynolds stress components exhibited a magnitude-amplification factor of 2–4 under the shock interaction, which could be related to the uplift of the large-scale vortical structures. The distribution of the mean TKE revealed a significant amplification between the sonic line and the outer edge of the separation bubble, while the wall-normal profiles exhibited an outer peak with the shock interaction, indicating a strong relevance to the separated shear layer and the enlarged main separation bubble. The TKE budget analysis showed that the effects of the shock impingement promoted

transportation in the outer layer, where the production was mainly balanced by turbulence transport and dissipation. It should be noted that the convection term cannot be ignored in the outer region. The anisotropy-invariant analysis showed increased isotropy at the bump summit, while wall turbulence was transferred to a two-component axisymmetric state around the reattachment point.

Decomposition of the skin friction demonstrated the leading role of the TKE production term $C_{f,T}$ across the bump region, with an exception found at the bump summit in case SF, where the predominance was overtaken by the spatial development term $C_{f,G}$. However, after passing through the shock interaction, $C_{f,G}$ made a negative contribution to the skin friction. A novel scale-decomposition method was applied to determine the contribution of the physical length scales to $C_{f,T}$. At the upstream turbulent boundary layer, the small-scale fluctuations produced a dominant contribution of 62.64% to C_f via the TKE production. In the downstream reattached boundary layer, an increased contribution of the large-scale structures was identified, which could be related to the strengthened vortical structures in the interaction region. In case SF, the small- and large-scale fluctuations, contributing 50.28% and 49.72%, respectively, were of almost equal importance to the skin friction. Importantly, the characteristic length scale of the fluctuations was greatly increased under the effects of the shock impingement in case WS, with the corresponding structures located much further outward wall-normal positions, and the contribution of the large-scale fluctuations in the outer region was more than 80%.

ACKNOWLEDGMENTS

The authors gratefully acknowledge the support of the National Natural Science Foundation of China (NSFC) under Grant No. 11972356.

AUTHOR DECLARATIONS

Conflict of Interest

The authors have no conflicts to disclose.

Author Contributions

Jiang Lai: Investigation (lead); Validation (lead); Visualization (lead); Writing – original draft (lead); Writing – review & editing (lead).
Zhaolin Fan: Supervision (lead); Writing – original draft (supporting);

Writing – review & editing (supporting). **Siwei Dong**: Validation (supporting); Visualization (supporting); Writing – original draft (supporting); Writing – review & editing (equal). **Xinliang Li**: Methodology (lead); Software (lead); Writing – original draft (supporting); Writing – review & editing (supporting). **Fulin Tong**: Investigation (equal); Methodology (equal); Project administration (lead); Software (equal); Supervision (equal); Validation (equal); Visualization (equal); Writing – original draft (equal); Writing – review & editing (equal). **Xianxu Yuan**: Investigation (equal); Methodology (equal); Supervision (equal); Validation (equal); Visualization (equal); Writing – original draft (equal); Writing – review & editing (equal).

DATA AVAILABILITY

Data related to this study are available from the corresponding authors by request (yuanxianxu@cardc.cn and 515363491@qq.com).

REFERENCES

- ¹A. Ferri, “Experimental results with airfoils tested in the high-speed tunnel at Guidonia,” Report No. NACA-TM-946, 1940.
- ²D. S. Dolling, “Fifty years of shock-wave/boundary-layer interaction research: What next?,” *AIAA J.* **39**(8), 1517–1531 (2001).
- ³P. M. Ligrani, E. S. McNabb, H. Collopy, M. Anderson, and S. M. Marko, “Recent investigations of shock wave effects and interactions,” *Adv. Aerodyn.* **2**(1), 427–449 (2020).
- ⁴H. Babinsky and J. K. Harvey, *Shock Wave-Boundary-Layer Interactions* (Cambridge University Press, 2011).
- ⁵D. V. Gaitonde, “Progress in shock wave/boundary layer interactions,” *Prog. Aerosp. Sci.* **72**, 80–99 (2015).
- ⁶N. T. Clemens and V. Narayanaswamy, “Low-frequency unsteadiness of shock wave/turbulent boundary layer interactions,” *Annu. Rev. Fluid Mech.* **46**, 469–492 (2014).
- ⁷S. Chan, N. T. Clemens, and D. S. Dolling, “Flowfield imaging of unsteady, separated compression ramp interactions,” AIAA Paper No. 1995-2195, 1995.
- ⁸S. J. Beresh, N. T. Clemens, and D. S. Dolling, “Relationship between upstream boundary layer velocity fluctuations and separation shock unsteadiness,” *AIAA J.* **40**, 2412–2422 (2002).
- ⁹J. Andreopoulos and K. C. Muck, “Some new aspects of the shock-wave/boundary-layer interaction in compression-ramp flows,” *J. Fluid Mech.* **180**, 405–428 (1987).
- ¹⁰F. O. Thomas, C. M. Putnam, and H. C. Chu, “On the mechanism of unsteady shock oscillation in shock wave/turbulent boundary layer interactions,” *Exp. Fluids* **18**, 69–81 (1994).
- ¹¹E. Toubert and N. D. Sandham, “Large-eddy simulation of low-frequency unsteadiness in a turbulent shock induced separation bubble,” *Theor. Comput. Fluid Dyn.* **23**, 79–107 (2009).
- ¹²S. Priebe and M. P. Martín, “Low-frequency unsteadiness in shock wave–turbulent boundary layer interaction,” *J. Fluid Mech.* **699**, 1–49 (2012).
- ¹³M. Grilli, P. J. Schmid, S. Hickel, and N. A. Adams, “Analysis of unsteady behaviour in shockwave turbulent boundary layer interaction,” *J. Fluid Mech.* **700**, 16–28 (2012).
- ¹⁴J. Fang, A. A. Zheltovodov, Y. F. Yao, C. Moulinec, and D. R. Emerson, “On the turbulence amplification in shock-wave/turbulent boundary layer interaction,” *J. Fluid Mech.* **897**, A32 (2020).
- ¹⁵N. A. Adams, “Direct simulation of the turbulent boundary layer along a compression ramp at $M = 3$ and $Re_\theta = 1685$,” *J. Fluid Mech.* **420**, 47–83 (2000).
- ¹⁶A. Smits and K. Muck, “Experimental study of three shock wave/turbulent boundary layer interactions,” *J. Fluid Mech.* **182**, 291–314 (1987).
- ¹⁷M. Wu and M. P. Martin, “Direct numerical simulation of supersonic turbulent boundary layer over a compression ramp,” *AIAA J.* **45**, 879–889 (2007).
- ¹⁸C. Helm, M. P. Martin, and P. Dupont, “Characterization of the shear layer in a Mach 3 shock: Turbulent boundary layer interaction,” *J. Phys.: Conf. Ser.* **506**, 012013 (2014).
- ¹⁹F. L. Tong, C. P. Yu, Z. G. Tang, and X. L. Li, “Numerical studies of shock wave interactions with a supersonic turbulent boundary layer in compression corner: Turning angle effects,” *Comput. Fluids* **149**, 56–69 (2017).
- ²⁰D. Cavar and K. E. Meyer, “Investigation of turbulent boundary layer flow over a 2D bump using highly resolved large eddy simulation,” *J. Fluids Eng.* **133**(11), 111204 (2011).
- ²¹Y. Tsuji and Y. Morikawa, “Turbulent boundary layers with pressure gradient alternating in sign,” *Aeronaut. Q.* **27**(1), 15–28 (1976).
- ²²V. Baskaran, A. J. Smits, and P. N. Joubert, “A turbulent flow over a curved hill. I. Growth of an internal boundary layer,” *J. Fluid Mech.* **182**, 47–83 (1987).
- ²³R. Balin and K. E. Jansen, “Direct numerical simulation of a turbulent boundary layer over a bump with strong pressure gradients,” *J. Fluid Mech.* **918**, A14 (2021).
- ²⁴D. Webster, D. Degraaff, and J. K. Eaton, “Turbulence characteristics of a boundary layer over a two-dimensional bump,” *J. Fluid Mech.* **320**, 53–69 (1996).
- ²⁵X. H. Wu and K. D. Squires, “Numerical investigation of the turbulent boundary layer over a bump,” *J. Fluid Mech.* **362**, 229–271 (1998).
- ²⁶V. Baskaran, A. J. Smits, and P. N. Joubert, “A turbulent flow over a curved hill. II. Effects of streamline curvature and streamwise pressure gradient,” *J. Fluid Mech.* **232**, 377–402 (1991).
- ²⁷A. A. Lawal and N. D. Sandham, “Direct simulation of transonic flow over a bump,” in *Direct and Large-Eddy Simulation IV*, ERCOFTAC Series, edited by B. J. Geurts, R. Friedrich, and O. Métais (Springer, Dordrecht, 2001), Vol. 8.
- ²⁸N. D. Sandham, Y. F. Yao, and A. A. Lawal, “Large-eddy simulation of transonic turbulent flow over a bump,” *Int. J. Heat Fluid Flow* **24**(4), 584–595 (2003).
- ²⁹F. Sartor, C. Mettot, R. Bur, and D. Sipp, “Unsteadiness in transonic shock-wave/boundary-layer interactions: Experimental investigation and global stability analysis,” *J. Fluid Mech.* **781**, 550–577 (2015).
- ³⁰F. L. Tong, D. Sun, and X. L. Li, “Direct numerical simulation of impinging shock wave and turbulent boundary layer interaction over a wavy-wall,” *Chin. J. Aeronaut.* **34**(5), 350–363 (2021).
- ³¹Y. Zhang, H. J. Tan, F. C. Tian, and Y. Zhuang, “Control of incident shock/boundary-layer interaction by a two-dimensional bump,” *AIAA J.* **52**(4), 767–774 (2014).
- ³²M. P. Martín, E. M. Taylor, M. Wu, and V. G. Weirs, “A bandwidth-optimized WENO scheme for the effective direct numerical simulation of compressible turbulence,” *J. Comput. Phys.* **220**, 270–289 (2006).
- ³³F. L. Tong, S. W. Dong, and J. Y. Duan, “Direct numerical simulation of 3D separation bubble in shock wave and supersonic boundary layer interaction,” *Acta Aeronaut. Astronaut. Sin.* **43**(3), 125437 (2022) (in Chinese).
- ³⁴P. Bookey, C. Wyckham, and A. Smits, “Experimental investigations of Mach 3 shock-wave turbulent boundary layer interactions,” AIAA Paper No. 2005-4899, 2005.
- ³⁵S. Pirozzoli and F. Grasso, “Direct numerical simulation of impinging shock wave: Turbulent boundary layer interaction at $M = 2.25$,” *Phys. Fluids* **18**, 065113 (2006).
- ³⁶S. Pirozzoli, M. Bernardini, and F. Grasso, “Direct numerical simulation of transonic shock/boundary layer interaction under conditions of incipient separation,” *J. Fluid Mech.* **657**, 361–393 (2010).
- ³⁷P. R. Spalart, “Direct simulation of a turbulent boundary layer up to $Re_\theta = 1410$,” *J. Fluid Mech.* **187**, 61–98 (1988).
- ³⁸X. H. Wu and P. Moin, “Direct numerical simulation of turbulence in a nominally zero-pressure-gradient flat-plate boundary layer,” *J. Fluid Mech.* **630**, 5–41 (2009).
- ³⁹M. Waandim, L. Agostini, L. Larcheveque, and M. C. Adler, “Dynamics of separation bubble dilation and collapse in shock wave/turbulent boundary layer interactions,” *Shock Waves* **30**(5), 63–75 (2020).
- ⁴⁰M. A. Mustafa, N. J. Parziale, M. S. Smith, and E. C. Marineau, “Amplification and structure of streamwise velocity fluctuations in compression corner shock wave/turbulent boundary layer interactions,” *J. Fluid Mech.* **863**, 1091–1122 (2019).
- ⁴¹V. Pasquariello, S. Hickel, and N. A. Adams, “Unsteady effects of strong shock wave/boundary layer interaction at high Reynolds number,” *J. Fluid Mech.* **823**, 617–657 (2017).

- ⁴²P. Dupont, S. Piponniau, and J. P. Dussauge, “Compressible mixing layer in shock-induced separation,” *J. Fluid Mech.* **863**, 620–643 (2019).
- ⁴³S. Pirozzoli and M. Bernardini, “Direct numerical simulation database for impinging shock wave/turbulent boundary-layer interaction,” *AIAA J.* **49**(6), 1307–1312 (2011).
- ⁴⁴J. L. Lumley and G. R. Newman, “The return to isotropy of homogeneous turbulence,” *J. Fluid Mech.* **82**, 161–178 (1977).
- ⁴⁵S. B. Pope, *Turbulent Flows* (Cambridge University Press, 2003).
- ⁴⁶F. L. Tong, J. Y. Duan, J. Lai, D. Sun, and X. X. Yuan, “Hypersonic shock wave and turbulent boundary layer interaction on a sharp cone/flare model,” *Chin. J. Aeronaut.* (in press) (2022).
- ⁴⁷M. Grilli, S. Hickel, and N. A. Adams, “Large-eddy simulation of a supersonic turbulent boundary layer over a compression-expansion ramp,” *Int. J. Heat Fluid Flow* **42**, 79–93 (2013).
- ⁴⁸F. L. Tong, J. Y. Duan, and X. L. Li, “Shock wave and turbulent boundary layer interaction in a double compression ramp,” *Comput. Fluids* **229**, 105087 (2021).
- ⁴⁹M. B. Sun, N. D. Sandham, and Z. W. Hu, “Turbulence structures and statistics of a supersonic turbulent boundary layer subjected to concave surface curvature,” *J. Fluid Mech.* **865**, 60–99 (2019).
- ⁵⁰V. C. Patel, W. Rodi, and G. Scheuerer, “Turbulence models for near-wall and low Reynolds number flow—A review,” *AIAA J.* **23**, 1308–1319 (1985).
- ⁵¹C. G. Speziale, R. Abid, and E. C. Anderson, “Critical evaluation of two-equation models for near-wall turbulence,” *AIAA J.* **30**(2), 324–331 (1992).
- ⁵²A. J. Smits, B. J. McKeon, and I. Marusic, “High-Reynolds number wall turbulence,” *Annu. Rev. Fluid Mech.* **43**(1), 353–375 (2011).
- ⁵³V. Adumitroaie, J. R. Ristorcelli, and D. B. Taulbee, “Progress in Favre Reynolds stress closure for compressible flows,” *Phys. Fluids* **11**, 2696–2719 (1999).
- ⁵⁴K. Fukagata, K. Iwamoto, and N. Kasagi, “Contribution of Reynolds stress distribution to the skin friction in wall-bounded flows,” *Phys. Fluids* **14**, L73 (2002).
- ⁵⁵W. P. Li, Y. T. Fan, D. Modesti, and C. Cheng, “Decomposition of the mean skin friction drag in compressible turbulent channel flows,” *J. Fluid Mech.* **875**, 101–123 (2019).
- ⁵⁶N. Renard and S. Deck, “A theoretical decomposition of mean skin friction generation into physical phenomena across the boundary layer,” *J. Fluid Mech.* **790**, 339–367 (2016).
- ⁵⁷D. Sun, Q. L. Guo, X. X. Yuan, H. Y. Zhang, and C. Li, “A decomposition formula for the wall heat flux of a compressible boundary layer,” *Adv. Aerodyn.* **3**, 33 (2021).
- ⁵⁸Y. T. Fan, W. P. Li, and S. Pirozzoli, “Decomposition of the mean friction drag in zero-pressure-gradient turbulent boundary layers,” *Phys. Fluids* **31**, 086105 (2019).
- ⁵⁹F. L. Tong, J. Y. Duan, and X. L. Li, “Characteristics of reattached boundary layer in shock wave and turbulent boundary layer interaction,” *Chin. J. Aeronaut.* **35**(6), 172–185 (2022).
- ⁶⁰Z. G. Zhang, F. L. Tong, J. Y. Duan, and X. L. Li, “Direct numerical simulation of supersonic turbulent expansion corner with shock impingement,” *Phys. Fluids* **33**, 105104 (2021).
- ⁶¹L. Agostini, M. Leschziner, J. Poggie, N. J. Bisek, and D. Gaitonde, “Multi-scale interactions in a compressible boundary layer,” *J. Turbul.* **18**, 760–780 (2017).
- ⁶²C. Cheng, W. P. Li, A. Lozano-Duran, and H. Liu, “Identity of attached eddies in turbulent channel flows with bidimensional empirical mode decomposition,” *J. Fluid Mech.* **870**, 1037–1071 (2019).
- ⁶³Y. C. Duan, Q. Zhong, G. Q. Wang, P. Zhang, and D. X. Li, “Contributions of different scales of turbulent motions to the mean wall-shear stress in open channel flows at low-to-moderate Reynolds numbers,” *J. Fluid Mech.* **918**, A40 (2021).